Title

Future Brake-by-Wire Smart Actuators: Enhancing Vehicle Control Systems for Collision Avoidance and Braking

Permalink

Author

Arasteh, Ehsan

Publication Date

2023

Future Brake-by-Wire Smart Actuators: Enhancing Vehicle Control Systems
for Collision Avoidance and Braking

By

Ehsan Arasteh
Dissertation

Submitted in partial satisfaction of the requirements for the degree of

DOCTOR OF PHILOSOPHY

in
Mechanical and Aerospace Engineering

in the
Office of Graduate Studies

of the
University *of* California

Davis

Approved:

_____

Francis Assadian, Chair

_____

Donald L. Margolis

_____

Shima Nazari

_____

Iman Soltani

Committee in Charge

2023

Dedicated to the relentless pursuit of knowledge, to the unwavering support of my loved ones, and to the countless possibilities that lie ahead.

Contents

List of Figures

List of Tables

Abstract

The automotive industry is in the midst of a shift towards electrification, with an increasing prominence of by-wire technologies. This thesis is dedicated to investigating the modeling, control, and parameter optimization of brake-by-wire actuators, with applications for both future autonomous and non-autonomous vehicles. To this aim, a modular control architecture is proposed to facilitate the integration of these actuators into vehicles.

The actuators are initially modeled through bond graph methodology. Subsequently, a cascaded control approach is employed to govern the intelligent actuators, with individual controllers designed using the Youla parameterization technique. Two distinct physical parameter optimization strategies are employed to enhance actuator responsiveness and energy efficiency. One approach is based on linear system optimization using transfer function, while the other centers around nonlinear system optimization. Comparative evaluations of the actuators are conducted using step and ramp tests. Finally, a direct comparison of the actuators within the proposed control architecture is carried out through a straight-line braking test scenario.

Acknowledgments

I am deeply grateful to many individuals whose support, guidance, and encouragement have been instrumental in the completion of this dissertation.

First and foremost, I extend my heartfelt gratitude to my thesis advisor, Prof. Francis Assadian. His unwavering dedication, insightful guidance, and profound expertise have been invaluable throughout this journey. His mentorship not only enriched the quality of my research but also motivated me to overcome challenges and strive for excellence.

I would also like to express my sincere appreciation to Prof. Margolis, Prof. Nazari, and Prof. Soltani for their invaluable contributions as members of my thesis committee. Their thoughtful insights, constructive feedback, and scholarly expertise significantly enriched the scope and depth of this work. Their commitment to fostering intellectual growth has been a source of inspiration.

I extend a special thank you to my family, especially my parents, whose unwavering support has been the cornerstone of my academic pursuit. Their belief in my abilities, patience during challenging times, and constant encouragement have been my driving force. I am truly fortunate to have them by my side.

In addition, I am grateful to all my friends and colleagues who have shared their insights, engaged in stimulating discussions, and provided me with a supportive network. Their camaraderie has made this academic endeavor even more rewarding.

This dissertation is the culmination of the efforts of many individuals, and I am deeply thankful for their unwavering support and guidance. The journey has been challenging yet immensely rewarding, and I am excited to carry forward the lessons and knowledge gained as I step into the next phase of my academic and professional journey.

Nomenclature

Acronyms

ABS Anti-lock Braking System.
ADAS Advanced Driver-Assistance Systems.

BBW Brake-By-Wire.

DoF Degrees of Freedom.

EHB Electro-Hydraulic Brake.
EMB Electro-Mechanical Brake.
ESC Electronic Stability Control.
EV Electric Vehicles.
EWB Electronic Wedge Brake.

HEV Hybrid Electric Vehicles.

MIMO Multiple Input Multiple Output.

NVH Noise, Vibration, and Harshness.

RGA Relative Gain Array.

SISO Single Input Single Output.
SMC Sliding mode controller.
SQP Sequential Quadratic Programming.

TCS Traction Control System.

Introduction

1.1 Reserach Goal and Scope

BBW systems are going to be the future of brake systems as they reduce cost and the number of parts (e.g. vacuum boosters and hydraulic parts), therefore, improving the system reliability. However, very little research has been done on the comparative analysis of these BBW systems in terms of different metrics such as efficiency, dynamic responsiveness, reliability, safety, and implementation cost. This research is attempting to find common metrics to compare and optimize different brake-by-wire systems and actuators. More specifically, the three most popular brake-by-wire actuators (EMB, EWB, and EHB) are studied in terms of energy efficiency and dynamic responsiveness metrics. However, other aspects will be considered in the comparison of these systems as well. By creating metrics, the actuator performance can also be compared based on their optimized set of parameters as well as their key differences.

On the vehicle side, we will investigate different possible topologies of BBW (i.e. combining different brake types in the vehicle). These proposed brake topologies will be compared in terms of the selected metrics.

The performance does not depend only on the brake components and topology but also on the designed control strategy. Therefore, it is equivalently important to investigate the impact of various control architectures and design the most appropriate architecture with re-usability and modularity for the proposed brake topologies. A few important use cases of this control architecture are the integration of friction brake-by-wire actuators with autonomous vehicle's control architecture and properly dealing with higher bandwidth BBW actuators in vehicle dynamics.

The goal of this project is to investigate and understand the impact of various brake-by-wire smart actuators and their topologies on the overall vehicle architecture and vehicle dynamics performance, safety, and reliability. To achieve these goals, the following questions should be answered:

- Which brake-by-wire hardware topology are being considered at the moment by automotive manufacturers and why?

- What are the appropriate metrics to be used for this comparative analysis?

- What is the most suitable modeling approach for brake-by-wire smart actuators?

- What is the most reusable, modular, and expandable control architecture for brake-by-wire systems that also guarantees vehicle dynamics safety and performance?

- What is the effect of control architecture on the brake-by-wire metrics? For example, how would the control architecture affect the energy consumption, reliability, and vehicle dynamics for the vehicle configurations?

- Which driving scenarios can benefit from brake-by-wire systems and their control architecture? What are the most appropriate control strategies for brake allocation between the wheels?

The novelty of this research is to design and develop a pragmatic smart brake-by-wire actuator including its control architecture by developing an understanding from a relative comparison of current brake-by-wire actuators through control design and optimization. To achieve this goal a few novel ideas are proposed in this thesis: To achieve this, the following novel contributions are made:

1. Use of a versatile control architecture for the BBW actuators that is modular and can be implemented in both autonomous and non-autonomous vehicles.

2. The use of robust control (Youla parameterization) for the controller actuators.

3. The optimization of brake-by-wire actuators' physical parameters using transfer function approach.

4. Comparison of different brake-by-wire topologies in the literature based on the chosen metrics.

1.2 Dissertation Outline

The outline of this dissertation is as follows,

- **Chapter 1** is the motivation, project scope, and literature review of brake-by-wire technologies. It sheds light on the problem statement and project aims, and evaluates existing literature to highlight gaps this research seeks to address.

- **Chapter 2** explains the control functional architecture of the brake-by-wire system used for autonomous and non-autonomous vehicles. It provides an understanding of the conventional systems, leading to an explanation of the architecture chosen for this thesis.

- **Chapter 3** discusses all the vehicle and tire modeling used in the simulation and discussions along this thesis. It explains all the models used in both simulation and control design.

- **Chapter 4** presents all the modelling efforts involving the brake-by-wire actuators. It outlines the mathematical foundations and assumptions made to derive the models and discusses the representation of these actuators' dynamics in the simulations.

- **Chapter 5** describes all the control strategies and designs from the high level all the way to the low-level and actuator side. It delves into the underlying theory and reasoning for the choice of control strategies, their implications, and how they contribute to the overall architecture of the brake-by-wire system.

- **Chapter 6** introduces an optimization methodology for brake-by-wire actuators and their physical characteristics by optimizing for the performance of these actuators in the loop. It poses an optimization problem that demonstrates how the optimal settings enhance these brake-by-wire performances and minimize their energy.

- **Chapter 7** presents all the results from the optimization methods explained in Chapter 6. Additionally, all the simulation results and comparisons of the brake-by-wire actuators and different topologies are presented and discussed. It provides an in-depth comparison of all the brake-by-wire topologies using the aforementioned optimization methodology.

1.3 Literature review of brake-by-wire technologies

X-By-Wire technologies are the future of the automotive industry due to the increasing demand for electrification, fuel efficiency and greenhouse gas emissions. Their electronic architectures and interface also make them a great candidate for autonomous and Hybrid Electric Vehicles (HEV) and Electric Vehicles (EV). Among all the necessary by-wire technologies, brake-by-wire systems are a priority due to their safety-critical nature in the vehicle [1]–[3].

Brake-by-wire systems can reduce component weight and allow the actuators to improve energy consumption. This can minimize fuel consumption and CO_2 emissions. Using sensors and control methods, caliper drag (which happens when the brake pad is not released completely once the brake pedal is released) can be eliminated; thus, making brake-by-wire technology even more energy efficient. Individual wheel braking and faster activation time can be combined with the vehicle's Electronic Stability Control (ESC) system to make the vehicle safer. The reliability of new actuators and the risk and cost associated with deploying new brake technologies are the main hurdles of brake-by-wire systems gaining popularity in the automotive industry [4].

1.3.1 Brake-by-wire actuators

Brake systems are categorized into wet and dry brakes. Wet brakes employ fluids for their operation, and dry brakes are usually purely mechanical systems. Electro-hydraulic brake systems are a type of wet brakes where the brake pressure is modified using pressure modulators that can be controlled electronically. The pressure source can be packaged in one centralized location for all four wheels like Bosch's first electro-hydraulic brake system. These types of brakes require an accumulator and a pump and usually a vacuum booster to maintain their high pressure throughout the braking operation. Dry brakes can also be realized in a few different configurations. Purely electro-mechanical brake utilizes a small motor, planetary gear set, and a roller-screw to move the brake pad [5]–[8]. However, this type of brake requires a 42 volt motor to operate and is energy intensive [4]. Electronic wedge brakes, on the other hand, use a wedge mechanism to create a system that draws the wedge pad inside the brake; therefore, requiring less energy to operate. They usually need a 14 V supply as opposed to 42 V of the electro-mechanical brake. However, this comes at the cost of more complicated mechanics and control [5], [8]–[16]. Vienna Engineering also came up with a similar idea using a crank-shaft mechanism that reduces the complexity of reduction gears and roller screws [17].

Purely dry brakes such as Electronic Wedge and VE brakes are going to be costlier than Electro-Hydraulic brakes since they are newer technologies and require more research and development before they become reliable enough to go into production. The other challenge for purely dry brakes is reliability since they have more electronic components and they all need to reliably perform in a harsh environment near the brake where vibration, shock, and high temperatures can have a significant impact [4].

On the other hand, EHB has already been in the market for a while. For example, there is an integrated electro-hydraulic brake system that utilizes an electro-mechanical actuator (similar to an electro-mechanical brake) as a modulator of a master cylinder. This electro-mechanical actuator uses a motor to rotate a gear mechanism and a ball-screw that pushes the piston. This axial force pressurizes the brake fluid inside the master cylinder and the pressurized brake fluid is then transferred to the wheel chamber using a high-pressure pipeline, where this pressure displaces the caliper (similar to an EHB). This integrated electro-hydraulic brake has the advantage of using most EHB parts which the automotive manufacturers are already familiar with and also removes the need for having a pump, vacuum booster, and accumulator. The result is a brake system that has a faster response than a normal EHB but still slower than pure EMB [18], [19]. It also seems that this type of brake actuator is gaining popularity among car manufacturers. Bosch GmbH developed the iBooster and ESP HEV (electronic stability program for hybrid and electric vehicles) which are integrated electro-hydraulic and hydraulic control unit (HCU) in 2013. In 2017, Continental AG introduced MK C1 which is a one-part integrated EHB with fast actuation and without any vacuum booster or accumulator along with emergency brake functionalities [20]. ZF TRW (with the IBC) and Hyundai Mobis (with iMEB) are among

the more recent suppliers who developed and manufactured integrated electro-hydraulic brake actuators.

1.3.2 Brake-by-wire smart actuator topologies

The configuration and combination of these brake-by-wire actuators have also been investigated.

Rear EMBs only configuration includes a hydraulic brake on the front and EMB in the rear (with integrated parking brake functionality). This has the advantages of simplified design requirements, using only 14 V power supply for EMB (since it's used in the rear axle), removing the parking brake, and safety and reliability features (since it also inherits from a mature hydraulic brake). There has been no configuration of *purely EMBs*, mainly since it requires a 42 V supply.

Front and rear EWBs has been investigated by Siemens VDO. The main issue was the loss of self-reinforcement once the direction of the rotation of tire changes such as when the vehicle is on an uphill and the vehicle is moving backward before going forward from a full stop. The actuators could draw a high current and may not hold the vehicle stationary. Siemens changes the braking direction for the front and rear axle exactly before the vehicle stop to mitigate this issue (the front axle brakes in the forward direction and the rear axle brakes backward). They also limit the current on the brake actuators. This works in most scenarios; however, on the rear-wheel-drive vehicles, this could lead to the driven axle pushing against a brake in a closed position and drawing high current at low speeds where there is a continuous change of directions. Additionally, there would be a need for an extra motor to perform electronic parking brake function (unless the forces are distributed between all four wheels during the parking which again poses a risk when holding a vehicle on a slope as mentioned) [4].

Rear EWBs only has also been prototyped by Mando; however, this would have the minimum advantage from the self-reinforcing mechanism as discussed. The company MOBIS prototypes a front EWB and rear EMB since higher braking force is required in the front. They mounted these brakes on a sedan vehicle and performed different ABS maneuvers. EWBs on the front would only need a 14 V supply and EMBs on the rear axle can implement parking brake function and would solve the issue of wheel direction changes. This configuration has a great advantage in terms of safety and failure modes (since there are two types of brakes used, which usually are not prone to the same modes of failure and decrease the probability of overall system failure); however, the cost of using two different types of brakes would be higher [4], [5].

Combination with Regenerative Braking The combination of these actuators with regenerative braking for Hybrid/Electric Vehicles has been studied as well [21]. Since brake-by-wires are easier and faster than the conventional disk brakes to independently

control each wheel, brake-by-wire systems integrate well with the regenerative braking and can save more energy. Gong et al. showed that using their electro-hydraulic brake system in an EV can significantly increase the energy recovery from regenerative braking [21]. Ko et al. proposed rear hydraulic brakes and front EWB in an HEV powertrain configuration. They then utilized the front axle electric motor in a series regenerative braking by blend in the front and rear axles friction brakes when needed. [22].

1.3.3 Objective Metrics for Brake-By-Wire Systems

To compare different systems, objective metrics are needed to measure each system's performance, robustness, and safety using the same criteria. Similar metrics have already been used in other automotive applications to optimize or compare different topologies. For example, Shankar et al. use different criteria for optimization and component sizing of plug-in hybrid electric vehicles. The objective functions in their optimization include all-electric range (AER), the CO2 emission from the drive-cycle, and the cost of components [23].

Gombert et al. provide some basic metrics for brake-by-wire actuators and their vehicle configurations which was discussed in Sections 1.3.1 and 1.3.2 [4]. This provides some background for objective metrics that need to be considered for BBW actuators. Yao et al. consider a multi-objective optimization with a few constraints for their combined electromagnetic and electronic wedge brake-by-wire actuator. The objective comprises of time to braking at an acceptable slew rate, maximum initial braking torque, and electric power of the DC motor. Their constraints include maximum power of the DC motor, brake slew rate, and maximum braking torque (maximum ground friction coefficient) [24]. Kwon et al. use a multi-objective formulation to optimize a caliper for the wedge brake. Their objective function includes the minimization of weight and the maximizing the caliper stiffness to maintain required stiffness while reducing the weight of the wedge brake. They then use the response surface model to optimize and find the best possible set of caliper parameters [25].

Metrics and metric-based optimization have also been used in the control architecture of brake-by-wire systems. Fengjiao et al. use multi-objective optimization for their control strategy of an electro-hydraulic brake system in an EV. Their objectives include maximizing the under wheel coefficient of friction on both rear and front wheels while also maximizing the regenerative energy. Constraints include battery charging power, motor peak torque, the relationship between braking stability and road adhesion condition [26]. Hielinger et al. use parameter optimization for an autonomous emergency braking system. Their cost function includes safety performance which is measured as the reduction of the impact speed [1], and customer acceptance which includes a sub-cost function for the brake profile and a sub-cost function for the distance (minimum distance between the vehicle and the

---

[1]the speed at which the vehicle might collide to the near obstacle if there is no collision the cost becomes zero

obstacle) [27]. Kelling et al. look at a distributed electronic and control architecture design for brake-by-wire systems and compares a conventional centralized architecture with a proposed fault-tolerant and distributed system in terms of safety and cost advantages [28].

1.3.4 Control Strategies for Brake-By-Wire Systems

Many researchers have used the sliding mode method to control the wheel slip for Anti-lock Braking System (ABS). Sliding mode controller (SMC) is a nonlinear robust control technique, it applies a non-continuous control law to force the system to operate on a sliding surface which defines the system's closed-loop dynamic. Compared to bang-bang control, SMC has the benefits of smaller actuation and added robustness. Anwar uses a sliding mode controller to control slip in a hybrid BBW system that resulted in a good slip regulation in low friction surfaces and a smooth ABS and reduced Noise, Vibration, and Harshness (NVH) in EHB systems [29]. Tanelli et al. used pseudo sliding mode mixed slip-deceleration (MSD) which continuously controls slip and deceleration while avoiding chattering and is robust to measurement noise and low sampling frequency [30]. However, SMC is not widely used in the automotive industry due to its complexity, difficulty of calibration, proper consideration of actuator delays, and lack of high frequency robustness. Actuators have delays that can make the sliding mode lead to chatter, energy loss, and excitation of unmodeled dynamics. However, this is not as much of a problem in the continuous control design [31]. Soltani et al. use a linearized model of EHB and synthesizes closed-loop shaping Youla parameterization for the wheel slip control. The stability and performance of the controller were tested on a HiL (hardware in the loop) setup [32].

The regenerative braking system may result in unstable braking during ABS maneuvers in the low mu conditions(regenerative braking can change the dynamic of the system which can lead to instability if it is not compensated). During ABS events, the regenerative braking is usually turned off [33]. Li et al. used a switching compensating control along with sliding mode to independently control the friction and regenerative brakes and were able to achieve a balance between braking performance (brake distance), reliability (fail-safe), and fuel economy [34]. He et al. used a multi-objective optimization to optimize the energy recovery efficiency and braking stability [35]. De Castro et al. used an optimization framework that is based on energy performance metrics, actuator constraints, and bandwidth to allocate the wheel torque between the regenerative braking and friction brakes [36]. Ehsani et al. define three different strategies for blending regenerative braking with friction brakes: Series braking (applying the regenerative braking first and then use friction brakes if necessary) with optimal braking feel, series braking with optimal energy recovery, and parallel braking. Series braking with optimal feel minimizes the stopping distance while optimizing the driver's pedal feel. Series braking with optimal energy recovery tries to recover as much energy as possible while satisfying the given deceleration demand. In the parallel brake system, friction brakes usually have a fixed force distribution ratio between the front and rear wheels while regenerative braking is also added to the rear wheels (regenerative braking can only

be applied to the driven wheels which in this case is assumed to be the rear wheel) [37], [38]. Ko et al. use a series braking strategy in a brake topology that includes rear hydraulic brakes and a front EWB in an HEV powertrain configuration. In this configuration, if the brake pedal is pressed less than a threshold, the braking priority is given to the regenerative braking and as the braking demand increases based on this given threshold, the front EWBs and then the rear hydraulic friction brakes are blended in. In case of emergency braking, a parallel braking strategy is activated [22].

The problems of brake system force distributions with regenerative braking capability are two-fold: the first is to choose the percentage of regenerative braking vs. friction braking at different times (actuator distribution) and the second is the force distribution between the four tires (brake force allocation) [19]. Zhang et al. control scheme prioritizes the stability performance of the vehicle over braking demand during braking-in-a-turn maneuver. Firstly, they allocate the brake forces between the front and rear axles. Then, these forces are distributed between the two wheels (inner and outer wheels) based on the longitudinal load transfer. Their independent braking force allocation for the BBW system shows a good balance between vehicle stability and braking performance [39]. Anwar uses a generalized predictive control method to develop a yaw stability controller for allocating the brake forces on a BBW system [40]. Hong et al. use a direct yaw moment calculation as a reference model to generate reference yaw rate and sideslip angle. A fuzzy logic controller is used to distribute the braking force at each wheel to generate the desired yaw rate [41]. Kim et al. use a genetic algorithm to obtain the optimal torque distribution between the regenerative braking and electro-hydraulic brakes for any desired yaw moment and given the road surface friction in a four-wheel-drive hybrid electric vehicle. They also use fuzzy logic control to track the desired yaw moment. Compared to a longitudinal only regenerative series braking, they show an increase in energy regeneration [42].

Control Functional Architecture

In this chapter, overall control architecture for controlling brake-by-wire actuators is explained which includes both autonomous and non-autonomous vehicles.

2.1 Software Stack of an Autonomous Vehicle and Motion Planner

The software stack for an autonomous vehicle typically includes multiple layers of software that interact with each other to enable the vehicle's autonomous operation. Figure 2.1 shows such architecture which consists of the following:

- Environment Perception: The perception layer is responsible for sensing the surrounding environment using various sensors, such as odometry, lidar, and radar. The perception layer processes the raw sensor data to extract meaningful information about the environment, such as the location and motion of other vehicles, pedestrians, and obstacles.

- Environment mapping and localization: This layer includes two parts: localization and mapping. The localization layer is responsible for estimating the vehicle's position and orientation in the world. This layer integrates information from various sensors, such as GPS, IMU, and wheel encoders, to determine the vehicle's pose with respect to a global reference frame. The mapping layer is responsible for constructing a map of the environment that the vehicle can use for navigation. This layer can use the data from the perception and localization layers to create a high-resolution map of the environment, including road geometry, lane markings, and traffic signs.

- Planning and Decision Making: The planning and decision-making layer is responsible for generating a feasible trajectory for the vehicle to follow, based on the current state of the vehicle and the surrounding environment. This layer uses various algorithms, such as probabilistic roadmaps, or search-based planning, to generate a collision-free and efficient trajectory that satisfies high-level objectives, such as minimizing travel time or energy consumption. Next, we will discuss the sub-layers within this layer.

- Control: The control layer is responsible for executing the desired trajectory generated by the planning and decision-making layer. This layer generates control inputs for the vehicle's actuators, such as the throttle, brake, and steering to follow the desired trajectory while accounting for uncertainties and disturbances. In the traditional automotive sense, this layer has a few components which will be discussed in the functional architecture section.
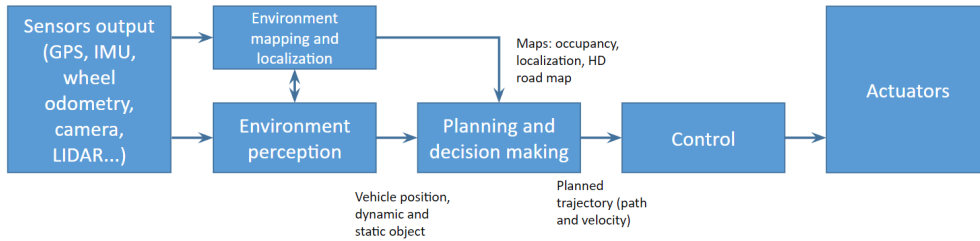
Figure 2.1: Autonomous Vehicle Software Stack

The motion planning layer is one of the critical components of the autonomous vehicle software stack, as it generates a feasible (collision-free) and efficient trajectory for the vehicle to follow, based on the current state of the vehicle and the surrounding environment. The other layers of the software stack, such as perception, localization, mapping, and control, interact with the motion planning layer to enable safe and efficient autonomous vehicle operation. Since the motion planning task is too complicated, it cannot be solved entirely in one block. A hierarchical path planning scheme is the most common approach that is being used (Figure 2.2). In this scheme, the mission planner focuses on the global and map-level navigation of the vehicle and chooses the vehicle's route. A standard algorithm used for this part of the planner is called A*, further explained in the motion planning section (section 2.3). The mission path information is then passed to the next part, the behavioral planner, which takes care of the vehicle's behavior in different environments and with respect to the other agents such as pedestrians and other vehicles. The behavioral planner decides when the vehicle needs to change lanes, stop at an intersection, yield when turning left, and other scenarios. The behavioral planner algorithms use different methods such as state machine, fuzzy logic, and reinforcement learning to handle this task. The last stage of motion planning is the local planner, which generates feasible collision-free paths from the current position to a local goal. Local motion planning algorithms will be discussed in the motion planning section 2.3.

The focus of this thesis is the control of brake-by-wire actuators using the functional architecture which will be explained in the later sections. To this end, we can assume that the motion planner has all the information about the environment and the obstacles around it and also perfect measurements of vehicle's states such as its position, velocity,
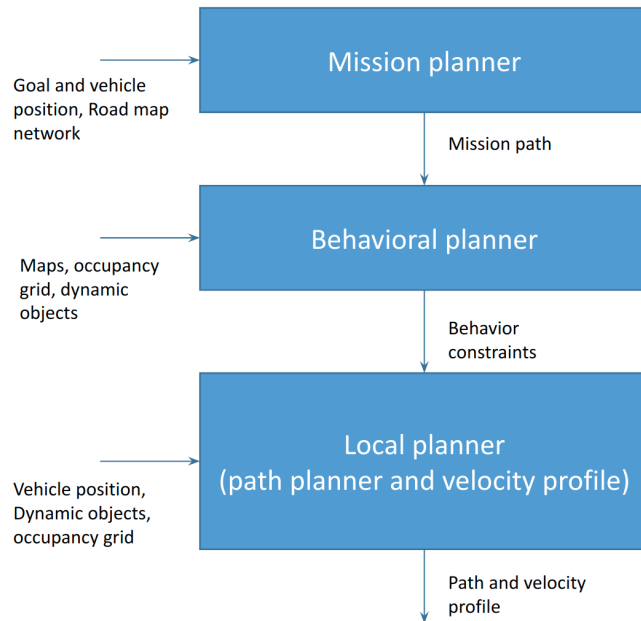
Figure 2.2: Hierarchical scheme of path planning in the autonomous vehicle

and acceleration. In the next section, we discuss the functional architecture used in this thesis for collision avoidance using brake-by-wire actuators.

2.2 Functional Architecture of Autonomous Vehicles

The functional architecture of an autonomous vehicle can be divided into several layers, each of which performs a specific set of functions to enable the vehicle's autonomous operation. Figure 2.3 shows such an architecture:

- Motion planning: As explained previously, the motion planner is a critical component of the system architecture of autonomous vehicles. It is responsible for generating a path that the vehicle will follow, taking into account a variety of factors such as the vehicle's speed, the road conditions, and other obstacles that may be present. The motion planner is typically designed using algorithms such as A* search or RRT (Rapidly-exploring Random Trees) that aim to find the most efficient path from the current location of the vehicle to the desired destination.

  In this case, the motion planner outputs a path that includes x and y coordinates along with heading angles ψ. It also provides a desired longitudinal velocity.

- Motion Control (trajectory following): Once a feasible trajectory is generated, the motion control layer is responsible for controlling the vehicle's motion along the trajectory. This layer tracks the desired trajectory while accounting for uncertainties and disturbances, such as road surface conditions, wind gusts, and sensor noise. The motion control layer generates overall steering angle and torque commands for the vehicle's longitudinal and lateral dynamics to follow the desired trajectory. The motion controller typically uses control methodologies such as Stanley controller [43] or model predictive control [44], to adjust the vehicle's trajectory and ensure that it stays on the desired path. The motion controller must take into account a variety of factors, including the vehicle's dynamics and road conditions, in order to make accurate control decisions. Other more robust control methodologies such as using Youla parameterization [45], [46] and H_∞ are explored by the researchers as well [47].

- Reference generator: The reference generation layer is responsible for prescribing a motion reference that determines the desirable vehicle's motion. This layer includes a vehicle model that produces desired longitudinal and lateral acceleration and yaw rate from the given steering angle and torque requests. Normally the vehicle model used for the reference generator is a bicycle model with a nonlinear tire model.

- High-level control: Once the prescribed motion signals have been determined by the reference generator, the high-level controller translates these motions into the generalized forces (Longitudinal (Fx), lateral (Fy), and C.G. moment around z (Mz)) that need to be applied to the vehicle in order to achieve those motions. One approach to designing a high-level controller for a vehicle is to use robust control techniques such as H-infinity control [48], [49] or Youla parameterization [50]. H-infinity seeks to minimize the effect of disturbances on the system while also ensuring good performance in terms of tracking the desired motions. The use of H-infinity control for the high-level controller of a vehicle can help ensure that the vehicle is able to follow the desired trajectories accurately and robustly, even in the presence of external disturbances such as wind or changes in road surface conditions. This can be particularly important for safety-critical applications such as autonomous vehicles or Advanced Driver-Assistance Systems (ADAS), where the ability to accurately follow the desired trajectory can be important.

- Control allocation: The control allocation layer is responsible for allocating the desired vehicle control inputs generated by the high-level control layer to the individual actuators that control the vehicle's motion. This layer takes into account the physical constraints of the vehicle's hardware, such as the maximum tire forces and actuator limits. The control allocation layer generates actuator commands that are consistent with the desired vehicle motion and the physical constraints of the vehicle's hardware. In the Figure 2.3, engine torque (τ_{engine}) is given to the engine, τ_{brake} is given to brake-by-wire actuators.

At the actuator level, the system architecture of autonomous vehicles becomes more complex. The actuator level includes components such as the brakes, the steering system, and the throttle. Each of these components must be carefully designed and calibrated to work together in order to ensure that the vehicle moves safely and smoothly along the path generated by the motion planner and controlled by the motion controller.

One important consideration in the design of the system architecture of autonomous vehicles is safety. Autonomous vehicles must be able to operate safely in a variety of different conditions, including adverse weather, unpredictable road conditions, and unexpected obstacles. Safety considerations must be integrated into every aspect of the system architecture, from the motion planner to the actuator level, in order to ensure that the vehicle can operate reliably and safely.

In conclusion, the system architecture of autonomous vehicles is a complex and multi-layered design that involves several components, including the motion planner, the motion controller, reference generator, high level control, control allocation and the actuator level. Each component must be carefully designed and calibrated to work together in order to ensure that the vehicle can move safely and smoothly along the path generated by the motion planner and controlled by the motion controller. Safety considerations must be integrated into every aspect of the system architecture to ensure that the vehicle can operate reliably and safely in a variety of different conditions. Both motion control and motion planning blocks act like the virtual driver of the vehicle as given by the blocks in Figure 2.1 and Figure 2.2. All the layers after can also be used in the non-autonomous vehicles as well since they relate to the physical layers of the vehicle as opposed to the virtual driver and autonomous stack of the vehicle as we will see in the next sections.
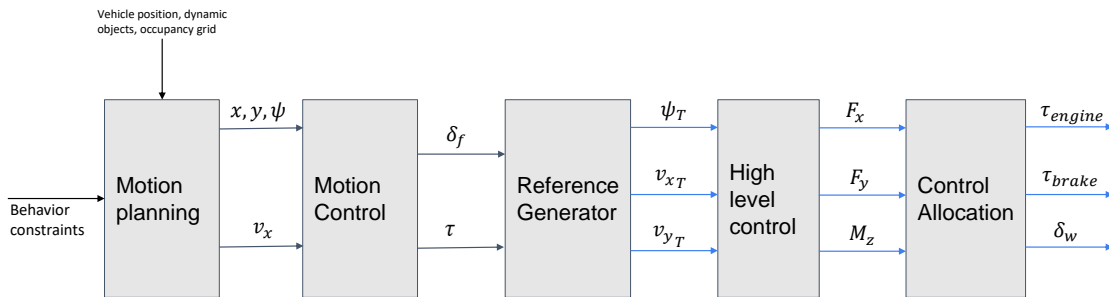
Figure 2.3: Function architecture of an autonomous vehicle from the motion planning to the actuator level

2.3 Motion Planning Algorithms for Autonomous Vehicles

Motion planning algorithms can be split into two primary methods of resolving the optimal path problem. The graph search approach generates a discrete map of the functional space and calculates the cost of travel to adjacent points from an initial point. The process is repeated from these adjacent points, generally in the direction that reduces the distance to a specified target point. Once the target point is reached, the path is selected using the lowest cost connections. This method provides the basis for algorithms such as A* and RRT (rapidly exploring random tree). A* is the first algorithm to mathematically compute an optimal path with a complete solution, meaning that the solution is verifiably optimal within the boundaries of the configuration space. As such, the solution becomes exponentially more difficult to compute with higher-order state spaces. To overcome this obstacle, sampling-based algorithms were developed that return a probabilistic solution. This may not always generate a perfectly optimal solution but does return the solution at a rate much faster than could be accomplished using a completion-based algorithm [51].

RRT (Rapidly Exploring Random Trees) and PRM (Probabilistic Roadmaps) are sample-based algorithms that generate realistic trajectories based on initialized constraints and develop a structure that minimizes a cost function to create the path. This is executed via the graph search method, using discrete points in a configuration space to determine the optimal trajectory. Using these tree structures, the algorithm can more quickly reach a solution by minimizing cost between the ends of each branch rather than verifying each discrete point in the configuration space. This does generate a solution that may be less than perfectly optimal since the solution is not checked at all points but produces a functionally similar path without a high computational cost. The graph search method requires a complete map of the configuration space to function correctly and generate a globally optimal path. This implies a constraint that the generated path may be locally suboptimal with incomplete information. Another consideration is that due to the discretization of the configuration space, a low-resolution localization can result in poor algorithm performance.

<div align="center">45 iterations   2345 iterations</div>
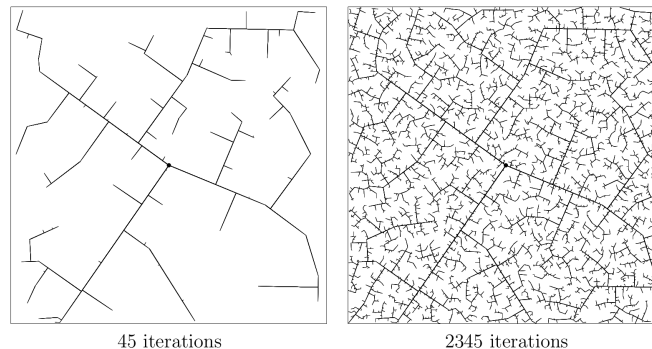
Figure 2.4: An example of Rapidly-Exploring Random Trees (RRTs) (Picture from [52])

The RRT and PRM utilize this discretized configuration space to search for an optimal path. PRM generates several randomly located sample points in the configuration space and then calculates the optimality of connections between these points. More advanced versions of this algorithm selectively compute connections to avoid calculations that would not contribute to an improved solution. RRT operates by generating a set of random branches and calculates the performance of each branch, passing through higher-performing branches to calculate the next set. RRT*, a more advanced version of RRT, checks local nodes between branches within each iteration. If a new branch can be formed between two previously found nodes, RRT* replaces that branch with the new branch. This results in the improved overall performance of the algorithm with a small additional computational cost. Both types of algorithms can be limited to generating branches that are within a deviation set that is realistic for an automobile; such that, time is not wasted calculating dynamically impossible solutions.

The variational method formulates a non-linear optimization problem that converges to a locally optimal path. Using a finite-dimensional vector, the variational method minimizes an associated cost function to optimize the resultant path. Instead of using a discrete mapping of points on the path, the produced lattice is derived from functions relating to the current position and a set of points at some distance away. The derived functions can be solved using either direct or indirect methods. Direct methods restrict the solution to a finite-dimension subspace, usually with a solution defined as a finite weighted sum of a basis function. This solution can be approximated using numerical integrators which satisfy constraints at collocation points or via pseudospectral methods which use a discrete-time interval and interpolate to evaluate trajectory between points. The latter method generally converges more quickly. Indirect methods utilize Pontryagin's Minimum Principle to determine optimality conditions of the path planning problem. While numerically difficult, this method reduces the dimensionality of the optimization problem.

One example of this method is the Conformal Lattice Planner (CLP) algorithm, which generates a lattice of potential realizable paths which interconnect a set of nodes and selects the path for which the cost function is minimized. The paths are generated with road geometry in mind, allowing for the algorithm to quickly search through the set of paths likely to yield an optimal result.[53] This method generates a locally optimal path in a short time frame but is constrained to paths defined by the lattice geometry. Additionally, using too few nodes on the configuration space can limit the performance of the algorithm.[54]

2.4 Functional Architecture of Non-Autonomous Vehicles

According to Kissai et al. there are multiple control architectures for controlling different actuators that affect the vehicle's behaviors, mainly:

- **Centralized Control**: In this architecture, all the actuators in the vehicle get controlled by one multi-variable global control block. This type of architecture is not
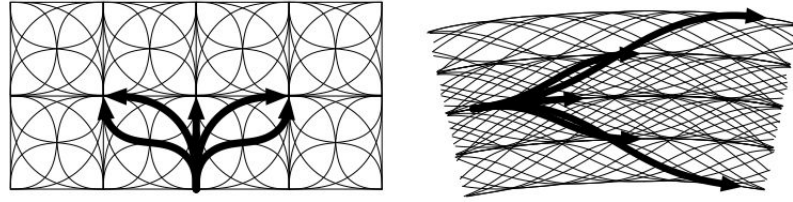
Figure 2.5: Conformal Lattice, Unoptimized (Left) and Optimized for Roadway Planning (Right)

fail-safe, and therefore any level of fail-safe redundancy for micro-controllers or power converters quickly escalates the cost of the control components. Considering this, a distributed control approach is favored, which can be achieved by supervisory control. Figure 2.6 shows the diagram for this type of architecture.
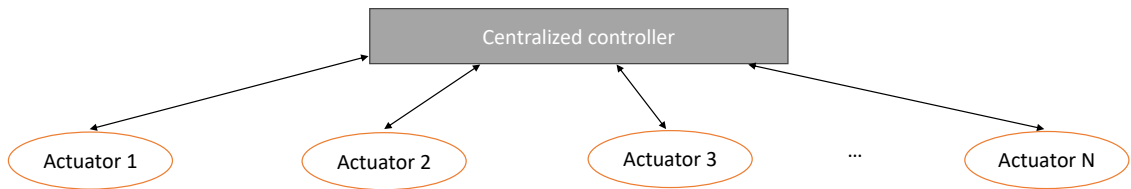
Figure 2.6: Centralized vehicle control architecture [55]

- **Supervisory Control**: In the supervisory control, there is a supervisor that sends the command to the individual controllers. Those controllers then send a command to the actuators. Figure 2.7 shows the diagram for this type of architecture.
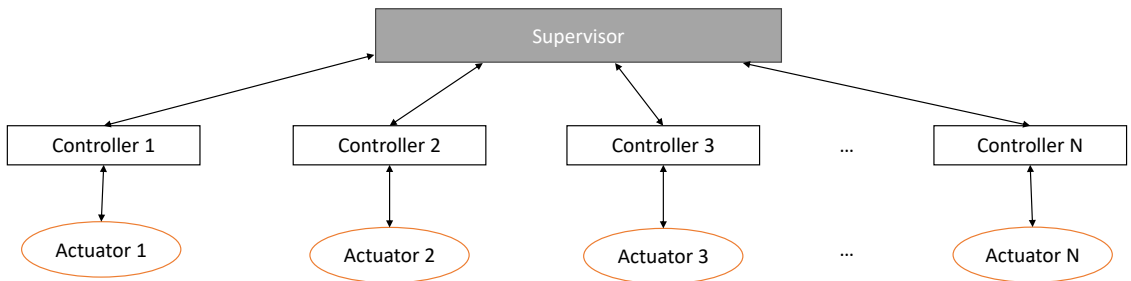
Figure 2.7: Supervisory vehicle control architecture [55]

- **Multi-Layer Architecture**: This architecture provides more flexibility and modularity than supervisory architecture. Each layer provides a specific functional requirement [55]. Because of its great flexibility and modularity, this is the most widely used architecture (e.g. [48], [50]). One example of this architecture is the one explained for the autonomous vehicles in section 2.2.
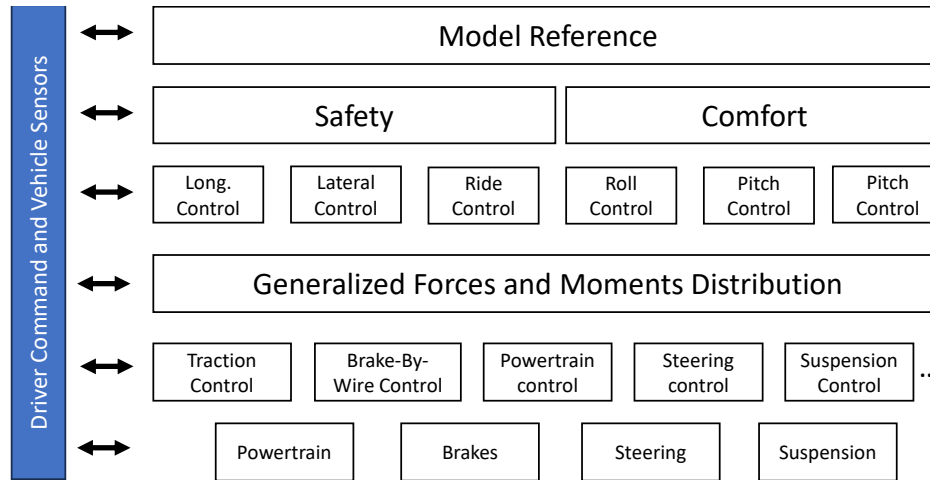
Figure 2.8: Multi-Layer vehicle control architecture [55]

2.5 Functional Architecture for the Brake-By-Wire Actuators

Based on the multi-layer architecture explained in the previous section, we propose the control functional architecture in Figure 2.9. Note that this is similar to the Architecture presented in Figure 2.3 for autonomous vehicles; however, the motion planning and motion control section of the architecture are removed since the vehicle is assumed to be operating by a human driver, and no autonomy is required. Instead, the driver's input to the steering system and accelerator/brake pedal for torque request are shown. δ_w and τ are the steering angle at the wheel and the brake torque request. The driver's steering input to the steering system generates the wheel's steering angle δ_f. For non-autonomous vehicles, when the driver pushes the brake pedal, it goes through a brake pedal look-up table which maps the driver's pedal input to the brake torque request (A similar map exists for accelerator pedal and the engine torque which is not shown in this architecture.). δ_f and τ are utilized as the inputs to reference generator to generate the inputs for the high-level control which then create generalized forces and moment. The control allocation then allocates appropriate brake torque reference to each wheel's brake-by-wire actuator ($\tau_{brake_{ref_{ij}}}$ where $i, j \in \{F, R\} \times \{L, R\}$). Each actuator then generates the brake torque that is being

requested. Note that this architecture can be used for autonomous vehicles by adding the autonomy stack and specifically motion planning and motion control blocks which eliminates the need for the driver's input.
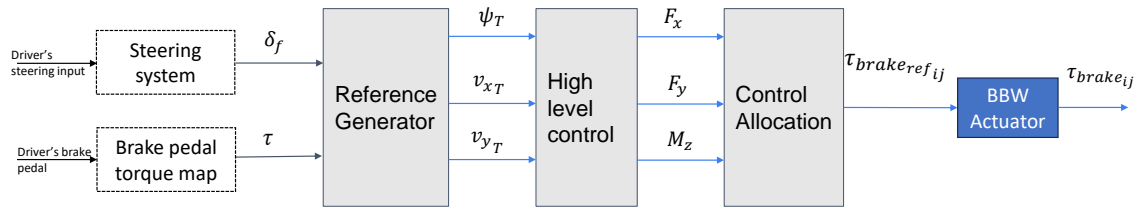
Figure 2.9: Functional architecture used to control the brake-by-wire actuators

Vehicle Modeling

Vehicle dynamics and tire modeling form a crucial part of understanding and optimizing the performance of various vehicular systems, including braking, steering, and suspension. These are essential for a comprehensive evaluation of the vehicle's ride and handling characteristics under diverse operating conditions. As vehicles become more sophisticated and incorporate advanced technologies like brake-by-wire actuators, the role of vehicle dynamics and tire modeling becomes even more critical, providing vital information that influences design, control, and overall performance enhancement of these systems.

This chapter focuses on tire modeling, including longitudinal and lateral modeling, as well as different vehicle models like the one wheel model, bicycle model, and extended bicycle model. Tire modeling, crucial to understanding the interactions between the vehicle and the road, plays a pivotal role in predicting the vehicle's handling characteristics. On the other hand, vehicle modeling is instrumental in providing simplified yet comprehensive representations of complex vehicular systems, enabling us to study and understand their behavior under varying conditions. The models discussed in this chapter, with different levels of complexity and accuracy, will be used not only to simulate the behavior of brake-by-wire actuators but also to design effective control strategies for these systems.

3.1 Tire modeling

Tire modeling is a crucial part of a vehicle dynamic model as it has a significant impact on vehicle behavior under different scenarios. There are three mechanisms involved in generating friction force between a rubber tire and the road: adhesion, deformation, and wear. To study these effects, various empirical and theoretical modeling techniques have been proposed by researchers.

3.1.1 Longitudinal tire modelling

The longitudinal force of the tire is proportional to the friction coefficient and the normal force.

$$F_{L_i} = \mu_i(\lambda) \cdot F_{z_i} \tag{3.1}$$

Where μ_i represents the longitudinal friction coefficient between the tire and the ground and F_{z_i} is the normal force exerted on each tire. There are different models for the longitudinal tire forces such as Pacejka magic tire formula [56], Dugoff [57], LuGre [58], and Burckhardt [59]. For the longitudinal tire modeling, we choose a simplified Burckhart model to represent the longitudinal tire model, for the sake of its simplicity and being able to capture longitudinal tire saturation well. The longitudinal friction coefficient is defined as

$$\mu(\lambda) = c_1 \cdot (1 - e^{-c_2\lambda}) - c_3\lambda \tag{3.2}$$

where c_1, c_2 and, c_3 are tire constants that depend on the road surface type (dry asphalt, wet asphalt, snow, ice) and λ are longitudinal wheel slip and during the brake, assuming positive slip ratio during braking, it is defined as

$$\lambda = \frac{u - R_w\omega_w}{|u|} \tag{3.3}$$

Where u is forward velocity of the vehicle, R_w is wheel's effective radius, ω_w is wheel's angular velocity. This relationship (Longitudinal friction Coefficient vs. Slip) is shown for a few of the road surfaces in Figure 3.1.
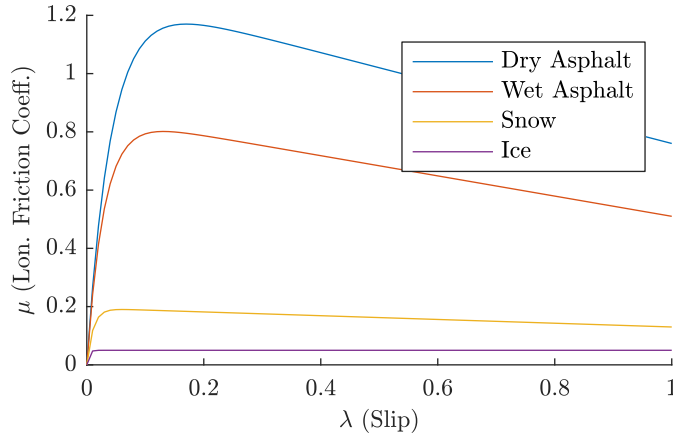
Figure 3.1: Longitudinal Friction Coefficient vs. Slip for different road surfaces using Burckhardt tire model

3.1.2 Lateral tire modelling

Linear tire model

The linear tire model assumes that tire forces are proportional to the slip angle. This usually works for small slip angles and when the tires are only operating in the linear region. In this case, front and rear tire lateral forces F_f and F_r are as follows

$$F_f = C_f \alpha_f \tag{3.4}$$
$$F_r = C_r \alpha_r \tag{3.5}$$

Where C_f and C_r are the front and the rear cornering stiffnesses and α_f and α_r are front and rear slip angles. The lateral tire slip angle, also known as the tire slip angle or the cornering slip angle, refers to the angle between the direction in which a tire is pointing and the direction in which it is actually moving. It is a measure of how much the tire is deviating from its intended path while cornering. Therefore, it is defined as the angle between its lateral velocity and longitudinal velocity.

$$\alpha_f = arctan(\frac{V_{c_f}}{V_{l_f}}) \tag{3.6}$$

$$\alpha_r = arctan(\frac{V_{c_r}}{V_{l_r}}) \tag{3.7}$$

Where V_{c_f} and V_{l_f} are lateral and longitudinal velocities of the front tire, and V_{c_r} and V_{l_r} are lateral and longitudinal velocities of the rear tire.

Pacejka lateral tire model

The Pacejka tire model, named after its creator Hans B. Pacejka, is a widely used semi-empirical model for describing the lateral behavior of vehicle tires. The model provides an approximation of the lateral forces and moments generated by a tire as a function of various inputs, including the slip angle, vertical load, and longitudinal slip. The lateral force generated by the tire can be calculated using the following equation:

$$F_y = D \cdot sin(C \cdot arctan(B \cdot \alpha - E \cdot (B \cdot \alpha - arctan(B \cdot \alpha)))) \tag{3.8}$$

where F_y is the lateral force acting on the tire, α is the lateral tire slip angle, and B, C, D are the parameters that depend on the tire properties and characteristics. The parameters B, C, D, and E are typically determined through experimental testing and fitting procedures to match the tire's behavior. These parameters account for the nonlinearities and complexities of the tire's lateral characteristics, such as the shape of the lateral force curve, saturation
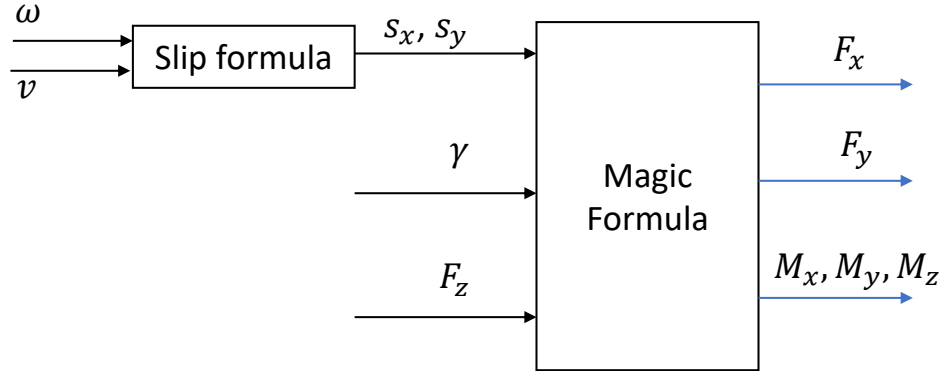
Figure 3.2: Pacjeka tire model inputs and outputs [61]

effects, and the transition from linear to nonlinear behavior. It's important to note that there are various versions and variations of the Pacejka tire model, such as the Magic Formula [56] and MF-tire/MF-Swift [60], which offer different levels of complexity and accuracy for modeling tire behavior. We will discuss the magic formula more in the next subsection.

3.1.3 Full tire modelling

Magic formula developed by Pacejka [56] consist of coefficients for each lateral force, longitudinal force, and self-aligning moment that the tire can produce at the contact patch and best fit the experimental data. These coefficients along with slip angles and camber angles are used to generate the forces for given normal forces. These models can accurately predict the tire behavior and are widely used in literature. The Magic Formula also incorporates other factors such as camber angle (tilt of the tire relative to the road surface) and longitudinal slip (difference between the tire's actual and ideal rotational speed). By considering these additional variables, the Magic Formula provides a more comprehensive tire model compared to a simple slip angle-based model. Figure 3.2 shows the inputs and outputs of Pacejeka tire model 3.2. ω is the wheel's angular velocity, v is the forward velocity of the tire, γ is camber angle and F_z is normal force of the tire. F_x, F_y, M_x, M_y, and M_z are longitudinal and lateral tire forces, longitudinal, lateral, and normal moments [61]. In this schematics, slip formula is Equation 3.9 which we will explain in the next section.

It's worth noting that there are variations and extended versions of the Magic Formula that introduce more parameters to account for additional tire characteristics, including combined slip (combined lateral and longitudinal slip), self-aligning torque, and more complex nonlinear behavior. These variations allow for more accurate tire modeling in different scenarios and applications.

This section describes a simplified version of Pacejka's Magic Formula. The longitudinal wheel slip ratio s_{ij_x} (where i is F (front) or R (rear) and j is R (right), L (left), denoted as $i, j \in \{F, R\} \times \{R, L\}$) and the wheel slip angle s_{ij_y} are computed from the vehicle longitudinal and lateral velocities in the tire frame v_{ijxt} and v_{ijyt} as described in (3.9). The small angle assumption is used to simplify the definition of the slip angle s_{ijy} as follows,

$$s_{ijx} = \frac{r_w \omega_{ij} - v_{ijxt}}{|v_{ijxt}|}, \text{ and } s_{ijy} = tan^{-1}(\frac{-v_{ijyt}}{v_{ijxt}}), \quad \text{where } i, j \in \{F, R\} \times \{R, L\} \qquad (3.9)$$

Note that s_{ijx} definition is positive longitudinal slip during the traction and negative during braking. Using the Pacejka's Magic formula with constant coefficients, the longitudinal and lateral forces, $F_{x_{ij}}$ and $F_{y_{ij}}$, in the tire frame are computed in (3.10) and (3.11) as follows,

$$\mu_{ij}(s_{ij}) = D \sin(C \tan^{-1}(B s_{ij})), \quad s_{ij} = \sqrt{s_{ijx}^2 + s_{ijy}^2} \qquad (3.10)$$

$$\mu_{ijx} = \frac{F_{x_{ij}}}{F_{z_{ij}}} = -\frac{s_{ijx}}{s_{ij}} \mu_{ij}(s_{ij}), \text{ and } \mu_{ijy} = \frac{F_{y_{ij}}}{F_{z_{ij}}} = -\frac{s_{ijy}}{s_{ij}} \mu_{ij}(s_{ij}) \qquad (3.11)$$

Where μ_{ij} is the under tire coefficient of friction for each tire and is dependent on s_{ij} which is combined slip and defined in Equation 3.10. We can use $F_{x_{ij}}$ and $F_{y_{ij}}$ of each tire in different vehicle models to accurately predict vehicle's longitudinal and lateral motions.

3.2 Vehicle modeling

To correctly predict the vehicle's motion under specific brake-by-wire actuators and different control algorithms, a correct model to capture the longitudinal and lateral model of the vehicle is required. Vehicle modeling can range from simple one-wheel models (that only model longitudinal dynamics) to complex full-vehicle models that replicate the behavior of the full vehicle. In the following subsections, all the vehicle dynamic models that are utilized in the simulation and control development in this thesis are explained.

3.2.1 One-wheel model

The wheel has rotational inertia and is connected to a point mass. For the preliminary studies of brake actuators and their algorithms (for example, the Anti-Lock Braking System, ABS, and Traction Control System (TCS)), this simple one-wheel model can be used and is
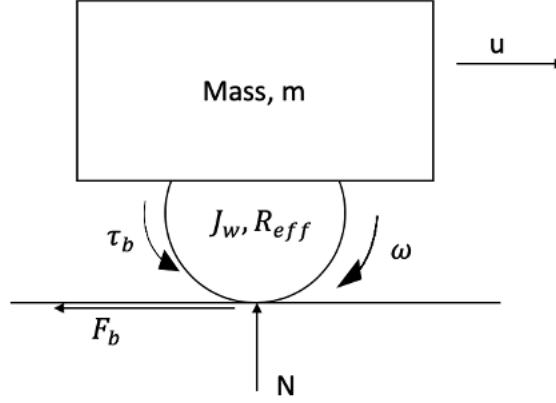
Figure 3.3: One-Wheel vehicle model

easy to implement later on a hardware-in-the-loop test. Models such as this can be used for studying longitudinal dynamics in the vehicle. Since it focuses only on the longitudinal dynamics of the vehicle, it is perfectly suited for studying brake-by-wire actuators and ABS technologies [62]. Figure 3.3 shows the schematics of this model. Equations 3.12 - 3.14 are the governing equations; where, J_w is the rotational inertia of the wheel, ω_w is the angular velocity of the wheel, F_b is the brake force, R_{eff} is the effective radius of the wheel, τ_b is the brake torque exerted on the wheel, u is forward velocity, m is the vehicle's total mass, N is normal force, and μ is the friction coefficient between the wheel and the ground (can be calculated using longitudinal tire model explained in section 3.1.1).

$$J_w\dot{\omega}_w = F_b R_{eff} - \tau_b \tag{3.12}$$

$$m\dot{u} = -F_b \tag{3.13}$$

$$F_b = \mu(\lambda) \cdot F_z \tag{3.14}$$

3.2.2 Bicycle model

The bicycle model is a widely used simplified representation of a vehicle. It is designed to capture the lateral dynamic behavior of the vehicle. Some models include longitudinal dynamics as well. The model consists of a rigid frame connecting a front wheel and a rear wheel, along with a steering angle that represents the angle between the front wheel and the vehicle's longitudinal axis. The lateral motion of the bicycle is modeled by the tire
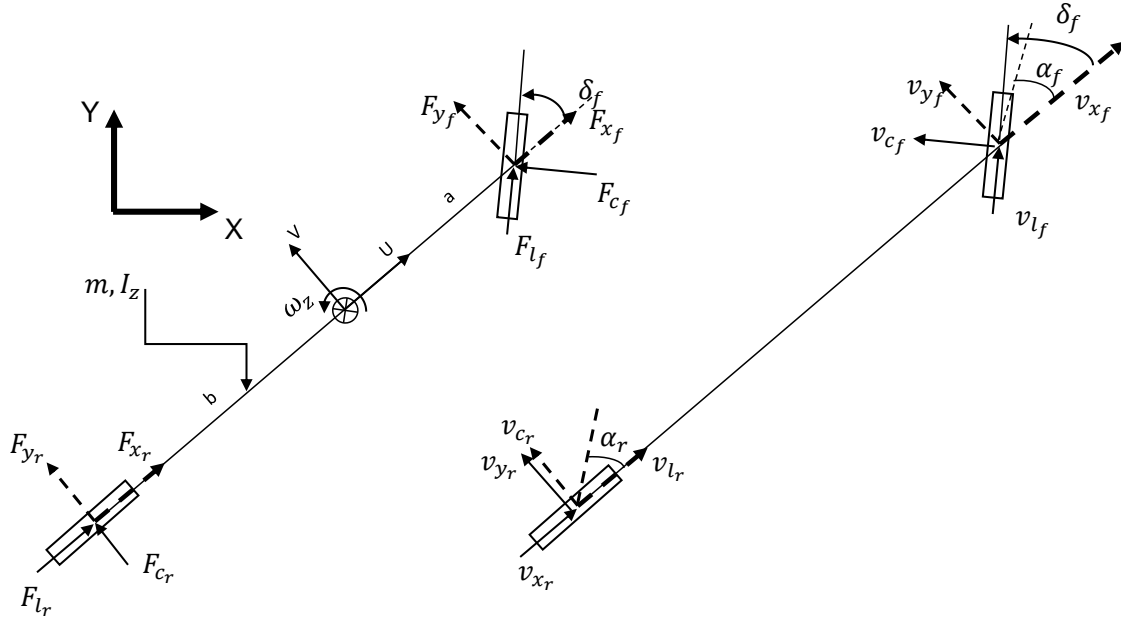
Figure 3.4: Bicycle model free body diagram and velocities

slip angle, which is the angle between the tire direction and the tire velocity vector. The longitudinal motion is modeled by the longitudinal slip, which is the difference between the speed of the wheel and the vehicle's speed.

The bicycle model is a useful tool for studying the handling and stability characteristics of vehicles, particularly in cornering maneuvers, where the lateral forces generated by the tires play a crucial role in the vehicle's stability.

Equations 3.15-3.20 represent the bicycle model's equations of motion.

$$m\dot{U} = m \cdot V \cdot \omega_z + F_{x_f} + F_{x_r} \tag{3.15}$$

$$m\dot{V} = -m \cdot U \cdot \omega_z + F_{y_f} + F_{y_r} \tag{3.16}$$

$$I\dot{\omega}_z = aF_{y_f} - bF_{y_r} \tag{3.17}$$

$$\dot{Y} = U sin(\psi) + V cos(\psi) \tag{3.18}$$

$$\dot{X} = U cos(\psi) - V sin(\psi) \tag{3.19}$$

$$\dot{\psi} = \omega_z \tag{3.20}$$

Where m, I_z, a, b, δ_f, ψ are the vehicle's mass, the moment of inertia around z, distance from the center of mass of the vehicle to the front axle, distance from the center of mass of the vehicle to the rear axle, front steering angle at the tire, and heading angle. ω_z, U, V, F_{y_f}, F_{y_r}, F_{x_f}, and F_{x_r} are yaw rate, longitudinal velocity, lateral velocity, front, and rear tire lateral force, and front and rear longitudinal force. X and Y are the longitudinal and lateral locations of the vehicle in the global coordinates. To get the tire longitudinal and lateral tire forces from the tire coordinates to the vehicle coordinates, we can use Equation 3.21 and 3.22 show this transformation.

$$F_{x_f} = F_{l_f}cos(\delta_f) - F_{c_f}sin(\delta_f) \tag{3.21}$$
$$F_{y_f} = F_{l_f}sin(\delta_f) + F_{c_f}cos(\delta_f) \tag{3.22}$$

Where δ_r is the rear tire angle, F_{l_f} and F_{c_f} are longitudinal and lateral tire forces in the tire coordinates.

For the front tire, using small angle approximation, we can approximate this to:

$$F_{x_f} \approx F_{l_f} - F_{c_f}\delta_f \tag{3.23}$$
$$F_{y_f} \approx F_{l_f}\delta_f + F_{c_f} \tag{3.24}$$
$$\tag{3.25}$$

For the rear tire, we simply have the following

$$F_{x_r} = F_{l_r} \tag{3.26}$$
$$F_{y_r} = F_{c_r} \tag{3.27}$$

To get the tire forces, we have to calculate the velocities at the tire coordinates. Equations 3.28-3.31 explain this relationship for the front and rear tires.

$$V_{c_f} = V_{y_f}cos(\delta_f) - V_{x_f}sin(\delta_f) \tag{3.28}$$
$$V_{l_f} = V_{y_f}sin(\delta_f) + V_{x_f}cos(\delta_f) \tag{3.29}$$

Where V_{c_f} and V_{l_f} are the longitudinal and lateral tire velocities in the tire coordinates. V_{x_f} and V_{y_f} are the longitudinal and lateral tire velocities in the global coordinates. Since δ_r is zero in front wheel steering vehicles,

$$V_{c_r} = V_{y_r} \tag{3.30}$$
$$V_{l_r} = V_{x_r} \tag{3.31}$$

Using the vehicle's motion, we also have Equations 3.32 and 3.33.

$$V_{y_f} = V + a \cdot \omega_z \tag{3.32}$$

$$V_{y_r} = V - b \cdot \omega_z \tag{3.33}$$

Now, we can substitute these velocities into the Equations 3.6 and 3.7 and get the slip angles for the front and the rear tires. We also linearize the velocity equations using small angle approximations. This is done in the Equations 3.34 and 3.35.

$$\alpha_f = arctan(\frac{V + a \cdot \omega_z - U \cdot \delta_f}{(V + a \cdot \omega_z) \cdot \delta_f + U}) \approx arctan(\frac{V + a \cdot \omega_z - U \cdot \delta_f}{U}) \approx \frac{V + a \cdot \omega_z}{U} - \delta_f$$

$$\tag{3.34}$$

$$\alpha_r = arctan(\frac{V - b \cdot \omega_z}{U}) \approx \frac{V - b \cdot \omega_z}{U} \tag{3.35}$$

Now, we can use the tire models developed in subsection 3.1.2 to calculate the lateral and longitudinal forces for the bicycle model.

3.2.3 Extended bicycle model

The extended bicycle model is the continuation of the bicycle model. In this case, the model includes all four tires. Extended bicycle model is a 7 Degrees of Freedom (DoF) model while a bicycle model is only 3 DoF model. Bicycle model with linear tires is usually used for linear analysis and designing controllers when a linear model of the vehicle is needed. An extended bicycle model is used as the platform for simulating the nonlinear behaviour of the vehicle model. Figure 3.5 shows the schematics for such a model. This model also includes tire rotational velocities. Assuming small angles, Equations 3.36-3.39 are the equations of motion governing this model.

$$m(\dot{U} - V\omega_z) = F_{FLx} + F_{FRx} + F_{RLx} + F_{RRx} \tag{3.36}$$

$$m(\dot{V} + U\omega_z) = F_{FLy} + F_{FRy} + F_{RLy} + F_{RRy} \tag{3.37}$$

$$I_{zz}\dot{\omega}_z = a(F_{FLy} + F_{FRy}) - b(F_{RLy} + F_{RRy}) + \frac{T}{2}(F_{FRx} - F_{FLx} + F_{RRx} - F_{RLx}) \tag{3.38}$$

$$J_w\dot{\omega}_{ij} = \tau_{ij} - r_w f_{ijxt}, \quad i \in \{F, R\}, \ j \in \{R, L\} \tag{3.39}$$

where m is the vehicle mass, I_{zz} is the yaw vehicle inertia, J_w is the wheel inertia, a and b are the distance between the center of gravity and the front and rear axle, respectively, T is the vehicle track width, and r_w is the wheel radius. The longitudinal and lateral tire forces F_{ij_x} and F_{ij_y} are expressed in the body-fixed frame attached to the chassis.
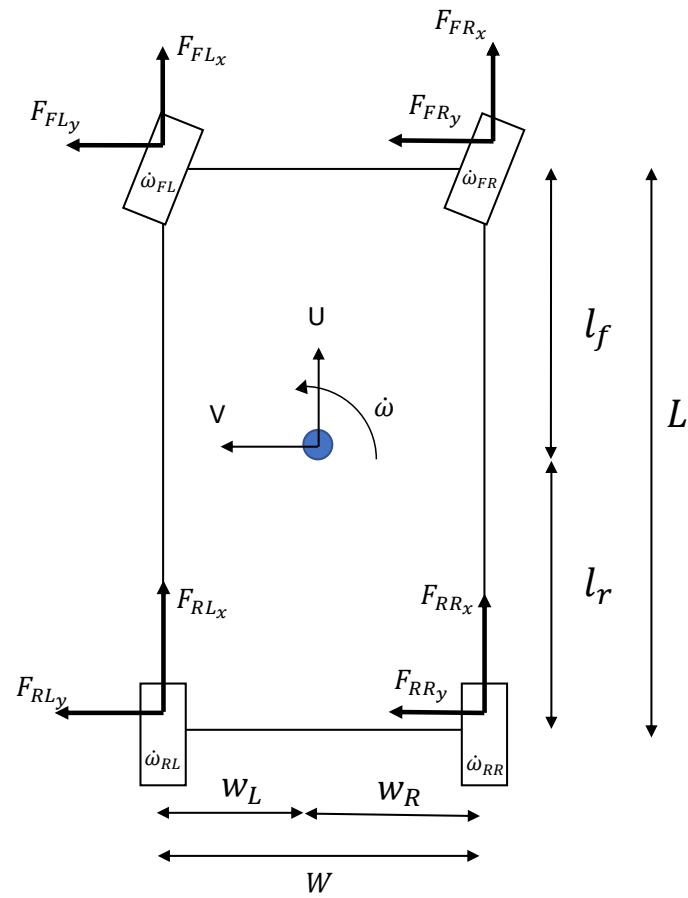
Figure 3.5: Extended bicycle model schematics

The tire model used in this model is the simplified Pacejka model presented in Section 3.1.3. All the lateral and longitudinal tire forces are calculated using Pacejka tire model. We still would require normal force of each tire to calculate those forces and because this vehicle model does not include suspension dynamics, the normal force cannot be computed from the suspension and tire vertical deflection. Therefore, we have to rely on algebraic forces to compute normal forces. Algebraic expressions can be used to describe the wheel load distribution in quasi-steady-state due to longitudinal and lateral acceleration.

$$F_{ijz} = F_{ijz}^0 \pm \Delta F_j^x a_x \pm \Delta F_i^y a_y, \ (i,j) \in \{F,R\} \times \{R,L\} \tag{3.40}$$

where the static load (F_{ijz}^0) and the load transfer terms $(\Delta F_j^x$ and $\Delta F_i^y)$ are

$$F_{ijz}^0 = \frac{mg(L - l_j)(W - w_i)}{LW} \tag{3.41}$$

$$\Delta F_j^x = \frac{mh(W - w_j)}{LW} \tag{3.42}$$

$$\Delta F_i^y = \frac{mh(L - l_i)}{LW} \tag{3.43}$$

Variables w_L and w_R denote the distance from the center of gravity of the vehicle to the left and ride sides; $W = w_L + w_R$ is the track width; l_F and l_R denote the distance from the center of mass to the front and rear axles; $L = l_F + l_R$ is the wheelbase; m is the total vehicle mass; g is the gravitational acceleration; h is the height of the center of mass with respect to the ground; and a_x and a_y are the vehicle longitudinal and lateral accelerations.

Brake-By-Wire Actuator modeling

In this chapter, a comprehensive examination of brake-by-wire actuators, including electro-hydraulic (EHB), electro-mechanical (EMB), and electronic wedge (EWB) brake systems, is undertaken. Each system is modeled based on the foundational principles of bond graph. The purpose of this chapter is to explain the technical aspects of these systems by describing their structural models and the intricate equations of motion that govern their operation. The schematics of EHB, EMB, and EWB brakes are shown in Figure 4.1a, Figure 4.2a and Figure 4.3a respectively.

Bond graph is a graphical modeling approach for dynamical systems based on the flow/exchange of power, and therefore, energy. Among many benefits of bond graphs, they are suitable for the systems with multiple energy domains such as mechatronic systems that usually include various electronic, electrical, mechanical, and hydraulic components [63]. Bond graphs are multi-energy domain and open architecture, which means one can easily add and expand the models with minimum effort compared to other modeling techniques. Furthermore, the monitoring and processing power and energy consumption of various components and parts are conducted with ease when using bond graphs. Given the mentioned benefits of this modeling technique, this method is adopted here to study and model BBW systems.

4.1 Electro-Hydraulic Brake

Figure 4.1a shows the schematics of an EHB. EHB model consists of a high-pressure source (master cylinder), hydraulic lines, build and dump valves, a brake cylinder chamber, and brake pads. The master cylinder provides pressure into the high-pressure line, controlled by the build and dump valves. Build and dump valves are considered to have varying states between their fully open and fully closed states. This is as opposed to the valves that can either be fully open or fully closed at a given time. In practice, these are solenoid valves that can be controlled with pulse width modulation. For the sake of initial comparison between these smart brake actuators, a vehicle model containing only one-wheel is utilized. When the pressure increases in the brake cylinder chamber, this pressure will move the

brake pad forward. This forward movement of the braking pad stops the brake disk as a result. Upon stopping, the dump valve opens, decreases the pressure, and releases the brake pads, bringing them back to their original position.

Based on the Figure 4.1a, the bond graph for EHB is presented in Figure 4.1b. Using the bond graph, we can come up with Equations (4.1)–(4.4) which represent the equations of motion for the EHB. q_{cyl}, p_p, x_{cal}, P_{in}, u_b, and u_d are the volumetric displacement of the cylinder fluid, momentum of the caliper, caliper displacement, pressure of the master-cylinder (high pressure input), duty ratio of build valve, and duty ratio of dump valve (between 0 and 1), respectively.

(a) EHB schematics [64]   **(b)** EHB bond graph
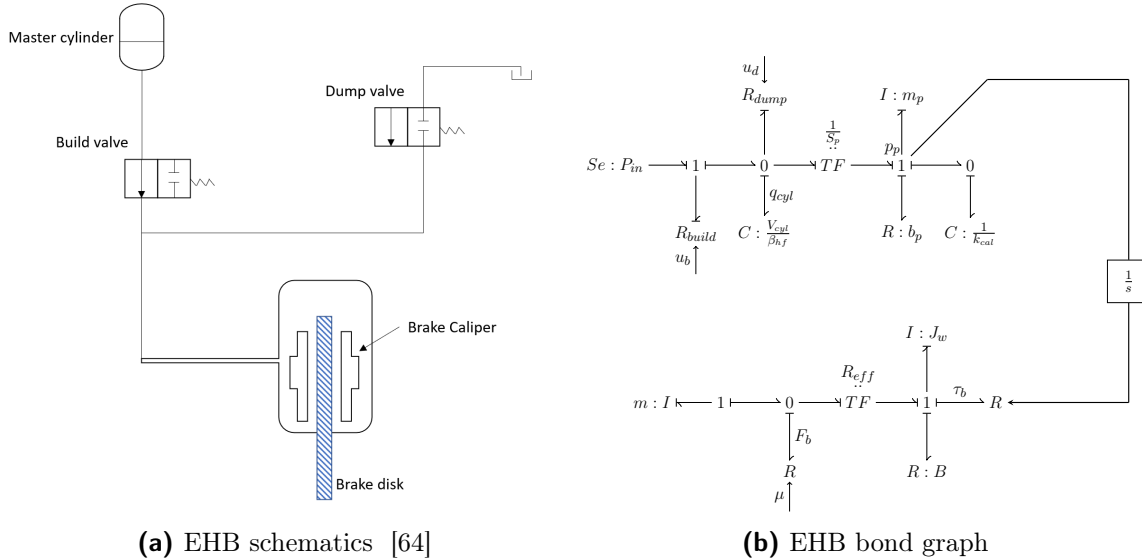
Figure 4.1: Schematics and bond graph of EHB

C_d, S_b, S_d, ρ, β_{hf}, V_{cyl}, S_p, b_p, m_p, x_0, and k_{cal} are the maximum flow coefficient of the valve, cross-sectional area of the build valve when fully open, cross-sectional area of the dump valve when fully open, density of the brake fluid, bulk modulus of the brake fluid, cylinder's volume, cylinder's cross-section surface, damping coefficient, brake pad's mass, brake clearance, and caliper stiffness, respectively [64]. Since these equations are highly nonlinear because of the valves, a linearized version, for the purpose of control development, is given in Equations (4.5)–(4.7). In this linearization, it is assumed that $u_d = 1 - u_b$, and this means that when one valve is open, the other is closed. EHB equations of motion

are as presented in 4.1-4.4.

$$\dot{q}_{cyl} = C_d S_b u_b \sqrt{\frac{2}{\rho}(P_{\text{in}} - \frac{\beta_{hf}}{V_{cyl}} q_{cyl})} - C_d S_d u_d \sqrt{\frac{2}{\rho}(\frac{\beta_{hf}}{V_{cyl}} q_{cyl})} - \frac{S_p}{m_p} p_p \tag{4.1}$$

$$\dot{p}_p = S_p \frac{\beta_{hf}}{V_{cyl}} q_{cyl} - b_p \frac{p_p}{m_p} - k_{\text{cal}} \ \max(x_{cal} - x_0, 0) \tag{4.2}$$

$$\dot{x}_{cal} = \frac{1}{m_p} p_p \tag{4.3}$$

$$P_{cyl} = \frac{\beta_{hf}}{V_{cyl}} q_{cyl} \tag{4.4}$$

4.1.1 Linearization of Equations of motion

Based on Equaions 4.1-4.4, we can linearize the equations of motion of the the EHB. Linearized EHB equations are presented in Equations 4.5-4.7. This linear stat-space representation can later on be used to design controllers for this actuator.

$$A = \begin{bmatrix} C_d S_b u_0 \sqrt{\frac{1}{2\rho}} \dfrac{-\frac{\beta_{hf}}{V_{cyl}}}{\sqrt{(P_{in} - \frac{\beta_{hf}}{V_{cyl}} q_{c0})}} - C_d S_d (1 - u0) \sqrt{\frac{1}{2\rho} \frac{\beta_{hf}}{V_{cyl}}} \frac{1}{\sqrt{q_{c0}}} & \frac{-S_p}{m_p} & 0 \\ S_p \frac{\beta_{hf}}{V_{cyl}} & -\frac{b_p}{m_p} & -k_{cal} \\ 0 & \frac{1}{m_p} & 0 \end{bmatrix} \tag{4.5}$$

$$B = \begin{bmatrix} C_d S_b \sqrt{\frac{2}{\rho}(P_{\text{in}} - \frac{\beta_{hf}}{V_{cyl}} q_{c0})} + C_d S_d \sqrt{\frac{2}{\rho}(\frac{\beta_{hf}}{V_{cyl}} q_{c0})} & 0 & 0 \end{bmatrix} \tag{4.6}$$

$$\begin{bmatrix} \dot{q}_{cyl} \\ \dot{p}_p \\ \dot{x}_{cal} \end{bmatrix} = A \begin{bmatrix} q_{cyl} \\ p_p \\ x_{cal} \end{bmatrix} + B \ u_b \tag{4.7}$$

4.2 Electro-Mechanical Brake

The EMB comprises a small electric motor, planetary gear set, ball-screw mechanism, brake pad, and caliper. A planetary gear set and a ball screw mechanism move the brake pad when the motor rotates. This movement will result in a clamp force that is denoted by F_{cl} as illustrated in Figure 4.2a. Utilizing this schematics, the bong graph for the EMB is drawn in Figure 4.2b.

Using this bond graph, the equations of motion for the EMB can be written using Equations (4.8a)–(4.8d). Note that the same nonlinear friction model has been used for the

EMB and EWB models. I_m, V_{in}, and ω_m are current, voltage input, and angular velocity of the shaft, respectively. L_m, R_m, K_t, J_m, D_m, N_s, N_p, and K_{cal} are the inductance of the electric motor, electrical resistance, electromotive force constant, total moment of inertia of the rotational parts (including the shaft and gears), axial viscous friction, planetary gear reduction ratio, ball-screw gear reduction ratio, and caliper stiffness, respectively [65].

EMB equations of motion are as follows:

$$\dot{I}_m = \frac{1}{L_m} \times (V_{in} - R_m \times I_m - K_t \times \omega_m) \tag{4.8a}$$

$$\dot{\omega}_m = \frac{1}{J_m} \times (K_t \times I_m - D_m \times \omega_m - \tau_f - N_p \times N_s \times K_{cal} \times \max(X_{cal} - x_0, 0)) \tag{4.8b}$$

$$\dot{X}_{cal} = N_s \times N_p \times \omega_m \tag{4.8c}$$

$$F_{Cal} = \begin{cases} K_{cal}\,(X_{cal} - x_0), & \text{if} \quad X_{cal} \geq x_0 \\ 0, & \text{otherwise} \end{cases} \tag{4.8d}$$

(a) EMB schematics   **(b)** EMB bond graph
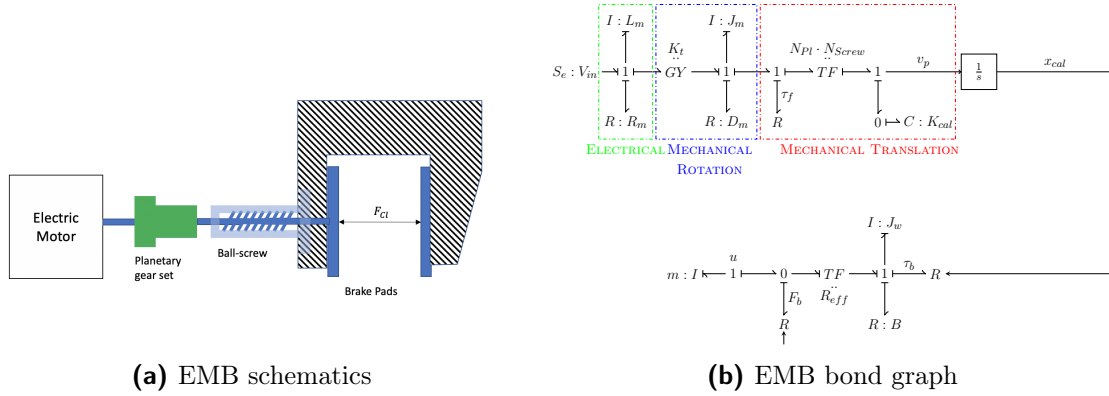
Figure 4.2: Schematics and bond graph of EMB

4.3 Electronic Wedge Brake

The EWB actuator converts the motor's rotation to a linear force on the wedge by using a planetary gear set (not depicted in the schematic) and a roller screw. The motor shaft's axial stiffness and resistance are also considered in modeling this actuator. K_{cal} represents the combined caliper stiffness and the stiffness between the wedge and the disk. This is similar to the EMB configuration, except that the caliper is shaped like a wedge, which, by inserting it inside the brake casing, creates a self-reinforcing mechanism. Figure 4.3a shows a schematics of this actuator and Figure 4.3b shows the corresponding bond graph for this actuator.

Using the bond graph for EWB, we can come up with the Equations (4.9a)–(4.9h) that show the equations of motion for the EWB, where N, q_{ax}, K_{ax}, D_{ax}, X_w, V_w, F_m, α, and μ_{cal} are combined gear reduction, shaft axial displacement, shaft axial stiffness, shaft axial viscous resistance, wedge displacement, wedge velocity, motor force exerted to the wedge, wedge angle, and friction coefficient between the pad and the wheel, respectively.

EWB equations of motion are as follows:

$$\dot{I}_m = \frac{1}{L_m} \times (V_{in} - i_m \times R_m - K_m \times \omega_m) \tag{4.9a}$$

$$\dot{q}_{ax} = LN\omega - \frac{V_w}{\cos(\alpha)} \tag{4.9b}$$

$$F_m = K_{ax}q_{ax} + D_{ax}\dot{q}_{ax} \tag{4.9c}$$

$$\dot{\omega} = \frac{1}{J_m}\{K_m I_m - D_m \times \omega - \tau_f - L \times N \times F_m\} \tag{4.9d}$$

$$\dot{V}_w = \frac{1}{m_w(1 + \tan^2(\alpha))} \times \{\frac{F_m}{\cos(\alpha)} + (K_{cal} \times X_w \times \tan(\alpha) \times (\mu_{cal} - \tan(\alpha))\} \tag{4.9e}$$

$$\dot{X}_w = V_w \tag{4.9f}$$

$$F_B = \mu_{cal}K_{cal}X_w \tan(\alpha) \tag{4.9g}$$

$$F_{Cal} = \begin{cases} K_{cal}(X_{cal} - x_0), & \text{if} \quad X_w \geq x_0 \\ 0, & \text{otherwise} \end{cases} \tag{4.9h}$$

τ_f is the lumped nonlinear frictions present in the shaft, planetary gears, and worm gear. The Lugre friction model has been used to model this nonlinear friction. The Lugre model is used for modeling the frictions in actuators since it offers a dynamical model which captures the dynamics very well while needing a lower number of parameters. Other types of friction models can be used as well to represent the frictions. Equation (4.10a) represents the Lugre friction model [66] where σ_0, σ_1, σ_2, ω_s, j, τ_c, and τ_s are the contact stiffness, damping coefficient of the bristle, viscous friction coefficient, Stribeck velocity, shape factor, Coulomb friction, and static friction, respectively. Equation (4.10d) shows that there is a linear relationship between the Coulomb friction and the clamping force, which is usually derived through experiment. As clamping force increases, the normal forces inside the gears increase as well, which results in increasing the friction torque [6]. Lugre dynamic friction

model for EMB and EWB is as follows:

$$g(v) = \tau_c + (\tau_s - \tau_c) \times e^{-(|\frac{\omega}{\omega_s}|)^j} \tag{4.10a}$$

$$\dot{z} = \omega - \frac{\sigma_0 \cdot |\omega| \cdot z}{g(v)} \tag{4.10b}$$

$$\tau_f = \sigma_0 \times z + \sigma_1 \times \dot{z} + \sigma_2 \times \omega \tag{4.10c}$$

$$\tau_c = C + G \times F_{Cal} \tag{4.10d}$$

(a) EWB schematics (cross-section view) [9]
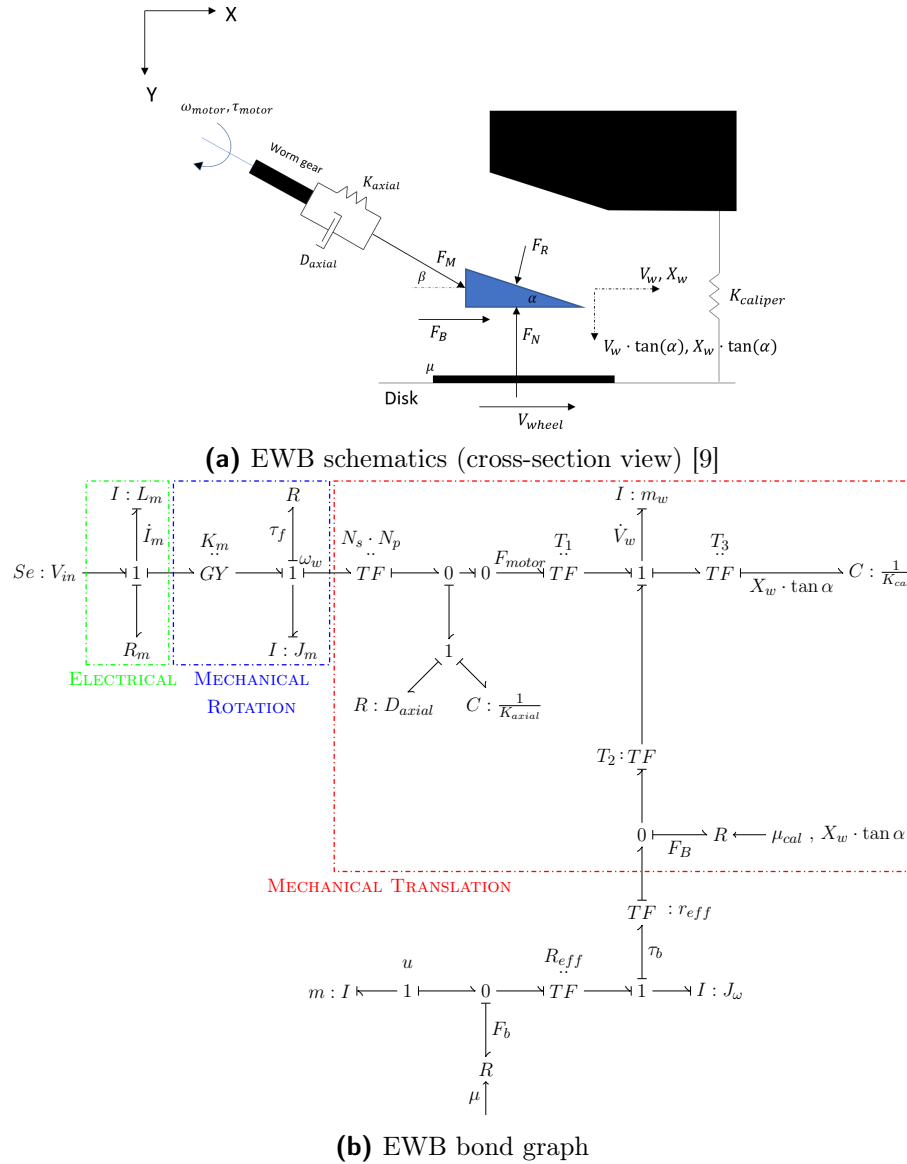
(b) EWB bond graph

Figure 4.3: Schematics and bond graphs of EWB.

Brake-By-Wire Control Strategies

In this chapter, we will discuss the layers involved in the control of BBW actuators shown in Figure 2.9 in more detail. We first go over Youla Parameterization approach explained in [67] which is then used in designing high-level controllers in section 5.3 and also design the low-level controllers for smart brake-by-wire actuators in section 5.5.

5.1 Youla Parameterization Robust control methodology

Robust control is a branch of control theory that deals with the design of controllers that can handle the presence of uncertainties in the nominal system model. In its early stages, this field was viewed as a reaction to perceived inadequacies of optimal control methods. As robust control principles have become mainstream, its methods have infiltrated the optimal control literature. Doyle provides a historical overview of the relationship between modern optimal control and robust control specifically H_∞ theory [68]. Youla et al. [69] and Kucera [70] independently came up with a controller design for Single Input Single Output (SISO) and Multiple Input Multiple Output (MIMO) plants that are not necessarily stable and extended the idea of Q factorization [71].

Youla et. al [69] present an analytical feedback design technique for single-input-output processes characterized by their rational transfer functions. The design procedure takes into account the topological structure of the feedback system and ensures asymptotic stability for the closed-loop configuration. The controller is designed using the Wiener-Hopf factorization of the plant transfer function, which separates the plant into minimum-phase and nonminimum-phase components. The minimum-phase part is used to design a stabilizing controller, while the nonminimum-phase component is used to design a compensator that deals with the nonminimum-phase zeros of the plant. The performance index used in the design procedure is the H-infinity norm, which ensures the existence of an optimal compensator for the system. The design procedure can handle unstable and nonminimum-phase processes, and it accounts for feedback sensor noise, disturbance inputs, and process saturation. Similarly, Kucera [70] uses an algebraic approach to the stability analysis and controller synthesis of discrete linear feedback systems. It provides a necessary and sufficient

condition for stability in algebraic form, and all compensators that stabilize the feedback system are found. Kucera offers a physical interpretation of the stability condition in terms of mode cancellations between the system to be compensated and the compensator. The controller synthesis is achieved by finding a compensator that satisfies the stability condition and achieves the desired closed-loop performance.

Youla parameterization is a robust control technique that allows for shaping the desired closed-loop transfer function (T), known as complementary sensitivity transfer function, while ensuring internal stability, disturbance rejection at low frequency, and sensor noise and unmodeled disturbance rejections at high frequencies. The main idea is to shape the closed-loop transfer function (T) with a transfer function called Youla (Y(s)), which when multiplied by the plant transfer function (G_p) would become the closed-loop transfer function (Equation 5.1). To have a good tracking performance at steady-state, T(s) should be one in magnitude at low frequencies, it should be small in magnitude at high frequencies to ensure high-frequency disturbance rejection.

$$T(s) = G_p(s) \cdot Y(s) \tag{5.1}$$

Therefore, according to Equation 5.1, we can shape the closed-loop transfer function (provided that we meet the interpolation conditions, for ensuring internal stability, mentioned below). It is worth noting that Youla transfer function is related to the actuator effort so having a low magnitude Youla, especially at high frequencies would keep the actuator effort low in a linear sense (since the transfer functions are linearized version of the plant).
The closed-loop transfer function (T(s)) is complementary to the sensitivity transfer function (S(s)) and the vector sum of these two transfer functions as given by (Equation 5.2) is known as an algebraic constraint. Therefore, this sensitivity transfer function should be small at low frequencies (to reject low-frequency disturbances) and equal to one in magnitude at high frequencies due to the algebraic constraint.

$$S(s) = 1 - T(s) \tag{5.2}$$

If G_p is stable, the feedback loop would be internally stable if and only if $Y(s)$ is selected to be a stable transfer function. In this regard, $Y_y(s)$, $S_y(s)$, $T_y(s)$, and $G_p \cdot S_y$ should all be stable to make the feedback loop internally stable. Consequently, to meet these conditions in case of an unstable pole (α_p) which is repeated n-times in the plant (G_p), Equations (5.3) and (5.4) define rational interpolation conditions, which must be met to enforce internal stability. If it is a single unstable pole (not repeated), Equation (5.3) is the only interpolation condition that needs to be satisfied:

$$T_y(\alpha_p) = 1, \quad S_y(\alpha_p) = 0 \tag{5.3}$$

$$\frac{d^k T_y}{ds^k}(\alpha_p) = 0, \quad \frac{d^k S_y}{ds^k}(\alpha_p) = 0, \quad \forall k \in [\![1, n]\!] \tag{5.4}$$

If there is a repeated non-minimum phase zero (α_z), zeros in the RHP (Right Half Plane), the interpolation conditions are met by Equations (5.5) and (5.6). If the unstable zero is only repeated once, Equation (5.5) is the only interpolation condition that must be satisfied [67]:

$$S(\alpha_z) = 1, \quad T(\alpha_z) = 0 \tag{5.5}$$

$$\frac{d^k S_y}{ds^k}(\alpha_z) = 0, \quad \frac{d^k T_y}{ds^k}(\alpha_z) = 0, \quad \forall k \in [\![1, n]\!] \tag{5.6}$$

Once we ensure that the conditions in the Equations (5.3)–(5.6) are met, we can acquire the controller using Equation (5.7):

$$G_c(s) = Y(s) \cdot S_y(s)^{-1} \tag{5.7}$$

5.2 Reference Generator
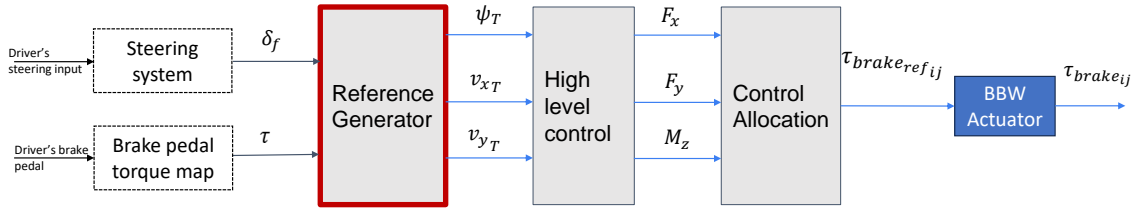
Figure 5.1: Reference Generator highlighted in the overall control architecture

The role of the reference generator or driver evaluator is to provide a set of desired outputs or goals that the control system should aim to achieve. Researchers use this method to make the vehicle behave the way it is desired [48], [50], [72]. Doumiati et al. use a reference generator to create a yaw rate target to stabilize a vehicle with active front steering and rear braking [72]. Tseng et al. use a bicycle model to create a target yaw rate based on the driver's steering input to stabilize the vehicle [73]. For the purpose of this thesis, we use a bicycle model with steering and torque inputs to generate the desired responses. This model is explained in 3.2.2. The only difference between that model and the model used in the reference generator is the torque input. To include brake torque, we would have to add Equation 5.8 as the definition of F_x in Equation 3.15.

$$F_{x_r} = \frac{\tau_b}{R_w} \tag{5.8}$$

Where τ_b is the total brake torque applied to the vehicle, R_w is effective radius of the wheel and F_{x_r} is longitudinal tire force.

5.3 High-Level Control
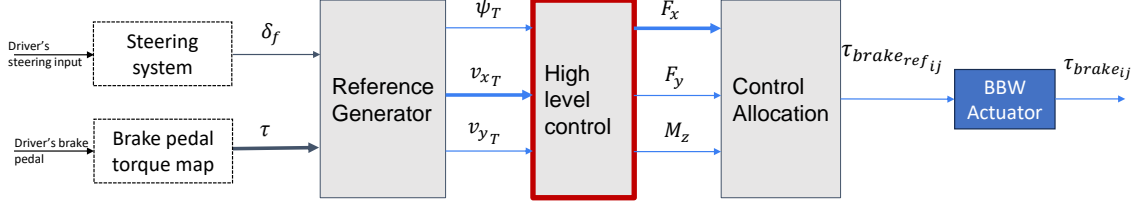
Figure 5.2: High-level control block highlighted in the overall control architecture

For the high-level control block, we first need to write down the equations of motion of the vehicle based on the generalized forces F_x, F_y, and M_z. This results in Equation 5.9.

$$\dot{V}_x = V_y \cdot \omega_z + \frac{F_x}{m} \tag{5.9}$$

$$\dot{V}_y = - V_x \cdot \omega_z + \frac{F_y}{m} \tag{5.10}$$

$$\dot{\omega}_z = \frac{M_z}{I_{zz}} \tag{5.11}$$

To create controllers for this MIMO system, we can linearize the system around an equilibrium point and reach Equation 5.12. V_{x_0}, V_{y_0} and ω_{z_0} are equilibrium points for longitudinal velocity, lateral velocity, and yaw rate and they are chosen to be 30 m/s, 2 m/s, and 0.1 rad/s respectively.

$$\begin{bmatrix} \dot{V}_x \\ \dot{V}_y \\ \dot{\omega}_z \end{bmatrix} = \begin{bmatrix} 0 & \omega_{z_0} & V_{y_0} \\ -\omega_{z_0} & 0 & -V_{x_0} \\ 0 & 0 & 0 \end{bmatrix} \begin{bmatrix} V_x \\ V_y \\ \omega_z \end{bmatrix} + \begin{bmatrix} \frac{1}{m} & 0 & 0 \\ 0 & \frac{1}{m} & 0 \\ 0 & 0 & \frac{1}{I_{zz}} \end{bmatrix} \begin{bmatrix} F_x \\ F_y \\ M_z \end{bmatrix} \tag{5.12}$$

The input is V_x, V_y, and ω_z and the output is the generalized forces and moment (F_x, F_y, and M_z). Therefore, in this case, $y = x$ which results in Equations 5.13 and 5.14 for C and D matrices.

$$C = \begin{bmatrix} 1 & 0 & 0 \\ 0 & 1 & 0 \\ 0 & 0 & 1 \end{bmatrix} \tag{5.13}$$

$$D = 0 \tag{5.14}$$

Using Equations 5.12-5.14, we can calculate the transfer function matrix for the MIMO plant as given in Equation 5.16. As it is shown, this matrix has off-diagonal elements. However, using Relative Gain Array (RGA) number of the matrix, we can show that the off-diagonal elements have near zero effect [50] and therefore we can decouple this system to 3 individual SISO systems. RGA of a MIMO system is a normalized form of the gain matrix that describes the input-output pairing. If the RGA is diagonal, that means that we can seperate the MIMO system into three SISO systems and control them separately since the cross coupling effects are zero.

$$RGA(G(s)) = G \cdot (G^{-1})^T \tag{5.15}$$

$$G_p(s) = \begin{bmatrix} \frac{s}{m \cdot (s^2 + \omega_{z_0}^2)} & \frac{\omega_{z_0}}{m \cdot (s^2 + \omega_{z_0}^2)} & \frac{V_{y_0} \cdot s - V_{x_0} \cdot \omega_{z_0}}{I_{zz} \cdot s \cdot (s^2 + \omega_{z_0}^2)} \\ \frac{-\omega_{z_0}}{m \cdot (s^2 + \omega_{z_0}^2)} & \frac{s}{m \cdot (s^2 + \omega_{z_0}^2)} & \frac{-V_{x_0} \cdot s - V_{y_0} \cdot \omega_{z_0}}{I_{zz} \cdot s \cdot (s^2 + \omega_{z_0}^2)} \\ 0 & 0 & \frac{1}{I_{zz} \cdot s} \end{bmatrix} \tag{5.16}$$

The individual SISO transfer functions are written in Equations 5.17-5.19. Now that we have the plant transfer function for each input and output, we can design controllers for each of them using Youla parameterization explained in Section 5.1.

$$G_{p_x} = \frac{V_x}{F_x}(s) = \frac{s}{m \cdot (s^2 + \omega_{z_0}^2)} \tag{5.17}$$

$$G_{p_y} = \frac{V_y}{F_y}(s) = \frac{s}{m \cdot (s^2 + \omega_{z_0}^2)} \tag{5.18}$$

$$G_{p_z} = \frac{\omega_z}{M_z}(s) = \frac{1}{I_{zz} \cdot s} \tag{5.19}$$

For Youla parameterization, we can choose the Equations 5.20-5.22 for each Youla transfer function for each model. This will result in a roll-off in Youla transfer function and a second order transfer function in closed-loop transfer function ($T_i = \frac{1}{(\tau_i \cdot s + 1)^2}$ $i \in \{x, y, z\}$). Figure 5.3 shows the Complementary (T), sensitivity (S), and Youla (Y) transfer functions for F_x, F_y and M_z loops.
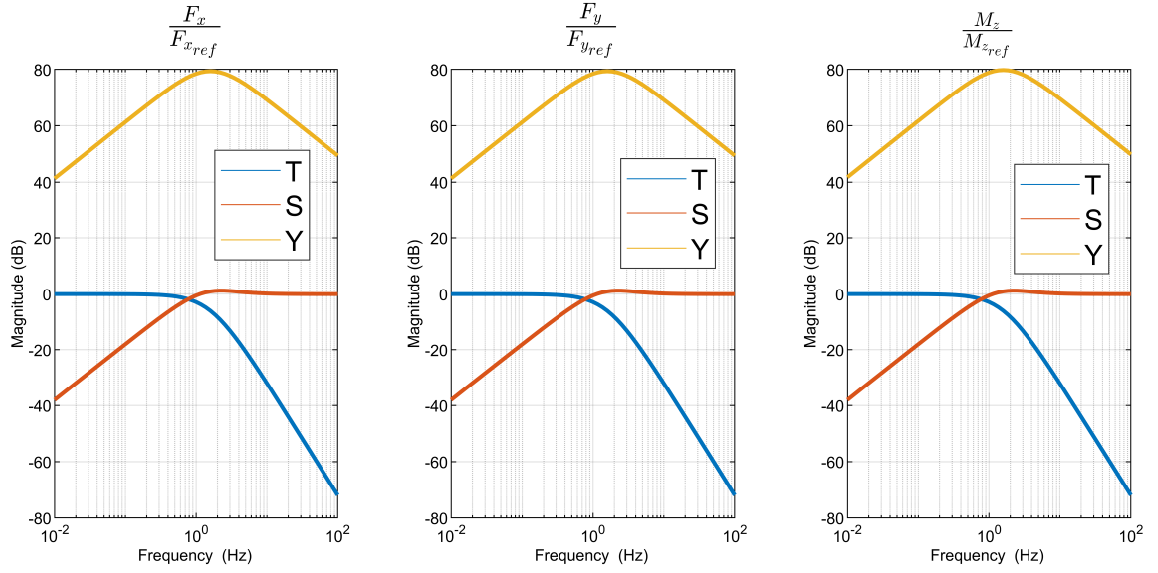
Figure 5.3: Complementary (T), sensitivity (S), and Youla (Y) transfer functions for F_x, F_y and M_z loops

$$Y_x = \frac{1}{G_{p_x}} \frac{1}{(\tau_x \cdot s + 1)^2} \tag{5.20}$$

$$Y_y = \frac{1}{G_{p_y}} \frac{1}{(\tau_y \cdot s + 1)^2} \tag{5.21}$$

$$Y_z = \frac{1}{G_{p_z}} \frac{1}{(\tau_z \cdot s + 1)^2} \tag{5.22}$$

After having the Youla transfer functions and T_i, we finally can calculate the controller using Equation 5.7.

5.4 Control Allocation
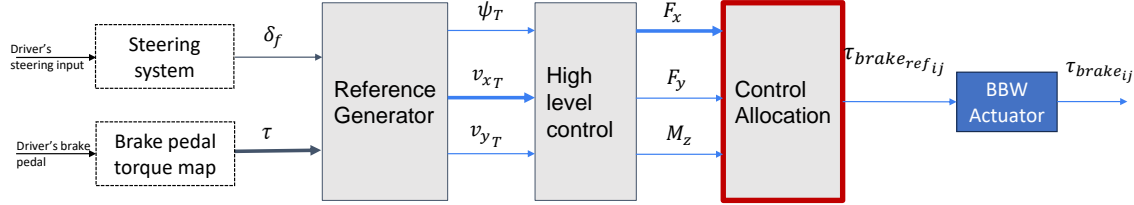
Figure 5.4: Control allocation block highlighted in the overall control architecture

The allocation strategy is used to distribute the CG forces and moments (F_x, F_y, and M_z) to all the actuators. In this case, we have four individual brakes that we would have to allocate the generalized forces and moment to them. This will result in a constraint optimization formulation. The cost function includes the target following of $u_{ref} = [F_x, F_y, M_z]$ and brake torque rate of change. For the target following, we must calculate the current generalized forces exerted on the chassis for which there is a mapping between each wheel brake torque and the vehicle states $X = [V_x, V_y, \omega_z]$. This map is represented as $f(X, \tilde{\tau}, \delta)$ where X is the vehicle states and $\tilde{\tau}$ is the vector of wheel brake torques $\tilde{\tau} = [\tau_{FL}, \quad \tau_{FR}, \quad \tau_{RL}, \quad \tau_{RR}]$ and δ is the steering wheel angle at the wheel. For the target following a weighted least square is used which is shown as $||u_{ref} - f(X, \tilde{\tau}, \delta)||_Q^2 = \frac{1}{2}(u_{ref} - f(X, \tilde{\tau}, \delta))^T Q(u_{ref} - f(X, \tilde{\tau}, \delta))$ where Q is a positive definite matrix for weighting each target. A weighted least square term for brake torque rate of change is also added. This is to limit the amount of rate of change of brake torque that is being asked from the brake actuators. This is represented as $||\Delta\tilde{\tau}||_R^2 = \frac{1}{2}\Delta\tilde{\tau}^T R\Delta\tilde{\tau}$ where $\Delta\tilde{\tau} = \tilde{\tau} - \tilde{\tau}^{prev}$ and $\tilde{\tau}^{prev}$ is the optimal brake wheel torque found in the previous timestamp.

This optimization would also include two constraints. The first constraint is the actuator limit constraint which sets an upper limit on the maximum brake torque that can each actuator provide. This constraint is written as Equation 5.26. The other constraint involves the friction ellipsoid for each tire. We must make sure that the braking torque for each tire does not exceed the maximum braking that it can provide for that surface and condition. This friction ellipsoid can be represented as Equation 5.23. To get the parameters for the tire ellipsoid, we can use the Pacejka tire formula explained in Chapter 3, Section 3.1.3. ($\bar{\mu}_x$, $\bar{\mu}_y$) is the center of the ellipsoid and $\Delta\mu_x$ and $\Delta\mu_y$ are the ellipse semi axes. More explanation on how these friction ellipse parameters are calculated from the magic formula is explained at [48]. In the optimization, this is shown as Equation 5.25.

$$\frac{(\mu_x - \bar{\mu}_x)^2}{\Delta\mu_x^2} + \frac{(\mu_y - \bar{\mu}_y)^2}{\Delta\mu_y^2} = 1 \tag{5.23}$$

Finally, the optimization will look like the following formulation.

$$\min_{\tilde{\tau}} \quad ||u_{ref} - f(X, \tilde{\tau}, \delta)||^2_Q + ||\Delta\tilde{\tau}||^2_R \tag{5.24}$$

$$\text{s.t.} \quad g(\tilde{\tau}) \leq 0 \tag{5.25}$$

$$0 \leq \tilde{\tau} \leq \bar{\bar{\tau}} \tag{5.26}$$

Since this is a quadratic cost with nonlinear constraints, we can use a Sequential Quadratic Programming (SQP) solver to solve this in the loop.

5.5 Brake-By-Wire low level actuators
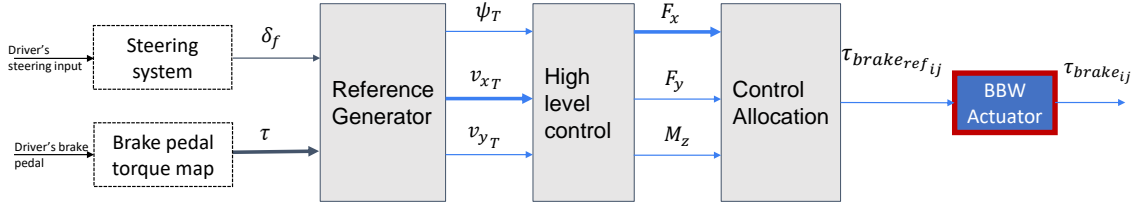
Figure 5.5: BBW low level actuators highlighted in the overall control architecture

In this section, we go over control strategies used for controlling an individual brake-by-wire actuator. The main methodology used for the motion control of brake-by-wire smart actuators in this thesis uses Robust control mainly Youla parameterization which was explained in section 5.1. In the next few sections, we will go over the details of the actuator control design for each EMB, EWB and EHB smart actuators.

5.6 Cascaded Control

Since the brake-by-wire smart actuators are Single Input Multiple Output (SIMO) problems, we consider the cascaded control scheme. Cascaded control enables SIMO systems to perform better and be more robust by being able to individually control each loop [74]. Therefore, the controllers were designed using cascaded control to mitigate different nonlinearities in the brake actuators (e.g., mechanical friction, pressure nonlinearities). Each inner closed-loop is an open-loop for their outer loop controller design. The controller design of each plant is conducted through the Youla parameterization approach, as discussed in the previous section. Figure 5.6 shows this cascaded control design for EMB and EWB actuators. In

the EMB and EWB, for the first loop, motor voltage is input, and motor current is the output. In the second loop, the motor's desired current is input, and the motor's angular velocity is output. Finally, for the outermost loop, the input is the desired motor angular velocity, and the clamping force is the output (the normal force of the brake pad on the wheel). The shaft's current and angular velocity can be measured directly and is readily available, but the clamping force must be estimated or measured with a force sensor. In the next chapter, we will discuss more about each control loop and their specific bandwidths. For example, Figure 6.1 shows an example of a cascaded control design for EMB/EWB for each loop.
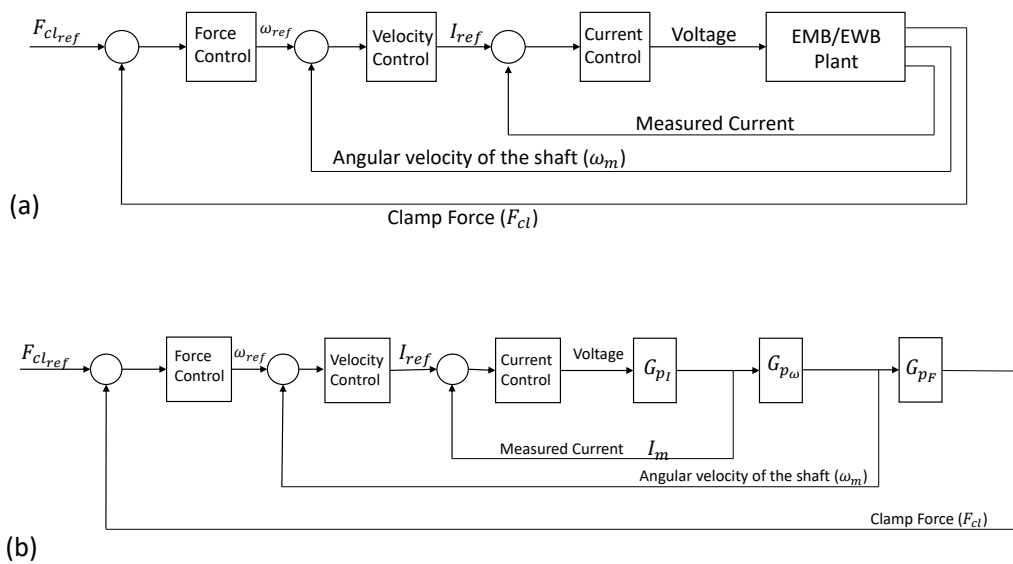
Figure 5.6: Cascaded control scheme for the EMB/EWB (**a**); The bottom Figure shows the decomposed system for control design (**b**).

5.7 Saturation and anti-windup

One important part of the EMB/EWB plant, which is not shown in Figure 5.6, is the current and voltage saturation. Current is saturated at ± 25 A, and voltage is set to saturate at ± 42 Volts. Because of these, the controllers might saturate and, therefore, results in loss of performance and/or instability. Anti-windup is a technique used in controllers with integral terms or when dealing with systems that have actuator saturation constraints. It is used to minimize the adverse effects of control input nonlinearities on closed-loop performance. There are several types of anti-windup schemes, and the choice of scheme often depends on

the specific requirements of the control system. Here are a few common types:

- **Conditional integral (Clamping)**: This method switches off the integration when a specific condition is met (saturation condition). There are several variations of this method:

    1. Limiting the integral term to a predefined value.

    2. Stopping the integration when the error is greater than a predefined threshold, which is when the process variable value is far from the set-point value.

    3. Stopping the integration when the control variable saturates.

    4. Stopping the integration when the control variable saturates and the control error and the control variable has the same sign [75].

- **Back-calculation**: Back calculation involves recalculating the integral term when the controller saturates. Specifically, the integral value is either reduced or increased (when the controller output is greater than its upper limit or less than its lower limit, respectively) by feeding back the difference between the saturated and unsaturated control signal. This technique includes an observer property that helps estimate the accurate state of the controller in cases where there is actuator saturation and the input of the plant does not align with it [75].

- **Model Recovery**: This is a more advanced scheme that involves augmenting the controller with an additional dynamic system designed to recover the performance of the unsaturated system. This can provide superior performance but is more complex to design and implement. For example, anti-windup bumpless transfer (AWBT) compensation can be applied to multivariable controllers of any structure and order. This approach unifies existing schemes for AWBT compensation under a general framework [76]. Zaccarian et al. propose a L_2 framework for the bumpless transfer in multi-controller system that have satuaration in them. The authors use LMI framework to come up with an anti-windup compesator [77]. Todeschini et al. use a similar LMI based method to come up with an anti-windup compensator for an electro-hydraulic brake-by-wire smart actuator that has multiple input saturations and dead-zone [78].

In this thesis, a simple back calculation anti-windup was used to address the current saturation and to mitigate this issue (Figure 5.7). There could also be another anti-windup for the voltage saturation; however, normally, the voltage does not reach saturation levels if the current saturation has been addressed. Furthermore, adding an extra anti-windup may result in limiting the bandwidth of the closed-loop system. In addition, other anti-windup strategies such as the one in [77] or [78], which is specifically for cascaded controllers, could have been utilized.
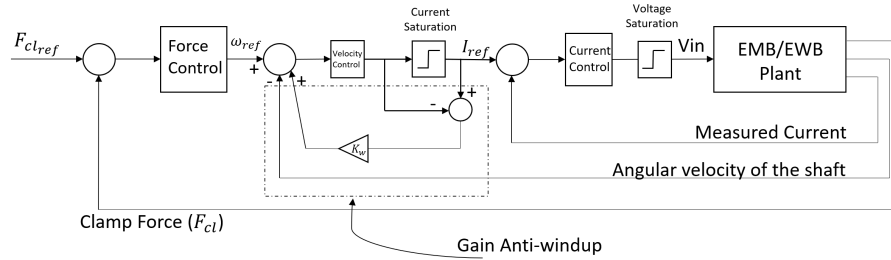
Figure 5.7: Anti-windup gain used to compensate for the current saturation.

5.8 EHB Control Scheme

In the EHB control design, a SISO controller was designed based on the linearized equations mentioned in Equations (4.5)–(4.7). The operating points taken for this linearization are $u_0 = 0.3$ and $q_{c0} = 0.3 \times q_0$. q_0 is the steady-state value of q_{cyl}. In addition, as mentioned before, it is assumed that $u_d = 1 - u_b$. This continuous control law works well when building and dumping the pressure in the cylinder chamber. However, in the case of keeping constant pressure during the steady-state, we might run into the issue of having both build and dump valves open partially at the same time and therefore losing some of the master cylinder's pressure which wastes energy. For example, $u_d = 0.7$ and $u_b = 0.3$ would hold the constant cylinder pressure, but this is not energy efficient as the pumps keep running. For this reason, a switching logic was added to the continuous Youla controller. This switching statement changes the values of u_b and u_d to zero once the clamping force error is within the desired threshold. Otherwise, it passes the same values from the controller to the plant as shown in Figure 5.8.
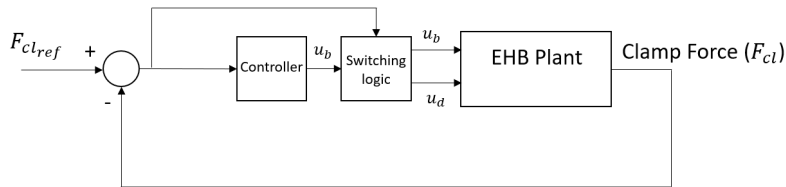
Figure 5.8: Control scheme for the EHB.

Brake-by-wire smart actuator optimization

In this chapter, a multi-objective optimization scheme for brake-by-wire actuators based on their transfer functions is considered. This optimization considers dynamic responsiveness and the actuator's effort as objective metrics.

6.1 Optimization: Using Linearized Plant Transfer Functions

After linearizing the plants, we can obtain their transfer functions. We then synthesize the controllers using the Youla parameterization technique discussed in section 5.1. There are a few assumptions made when designing the controllers during the optimization process. Controllers are designed to create closed-loop transfer functions to be in a certain form. Equations (6.1), (6.2), (6.4), (6.6a), (6.6b) , (6.8), (6.9a) and (6.9b) describe the form of plant transfer function (Gp), Youla transfer function (Y), and closed-loop transfer function (T) for the first, second, and the third loop of EMB (EWB follows a similar control design pattern, and EHB follows the same pattern, but it only has one control loop, and therefore, the design choice is similar to the one in Equation (6.2)). The goal here is to design a closed-loop transfer function with the frequency shape of a second-order Butterworth filter and add extra first-order filters whenever necessary. The Butterworth filter has a few desirable behaviors that make it a great candidate: it has a maximally flat magnitude region and it rolls off at a specific tuneable frequency with a slope of -20 db/decade. For example, in Equation 6.6a, the inverse of the second loop transfer function has a s in the numerator.. To meet the BIBO stability condition, we cannot directly cancel this s in the numerator with a pole located at zero, hence, we add a low pass filter to the Youla transfer function ($\frac{1}{s+W_1}$) where W_1 , chosen to be a small value, is the pole for the filter that is added to the Youla transfer function. This can be chosen in such a way that it does not affect the bandwidth of the closed-loop system. In this equation, G'_{p2} represents the plant transfer function of the second loop without the s in the numerator ($G'_{p2} \cdot s = G_{p2}$). Moreover, in the case of Equation 6.9a, a repeated first-order transfer function was added to the Youla transfer function to make this transfer function proper (G_{p3} is a fourth-order transfer function; for simplicity, we choose to use first-order poles. N-th order Butterworth filter could also be

used in this case). More details on the design of these controllers are provided in [79]. It should be noted that ω_{n_1}, ω_{n_2}, and ω_{n_3} are chosen for each loop to have a specific bandwidth (ω_{n_1}, ω_{n_2}, and ω_{n_3} are the Butterworth filter's cut-off frequencies for the different added Butterworth filter to Youla transfer functions). In the case of EMB, this is 200 Hz, 10 Hz, and 2 Hz for the first, second, and last loop, respectively. For the EWB, they are chosen to be 500 Hz, 400 Hz, and 2 Hz. Finally, for EHB, it is chosen to be 2 Hz. Therefore, all of the brake-by-wire actuators have the same final closed-loop of 2 Hz for the clamp force loop. This is a deliberate choice to make sure all the brake-by-wire actuators have the same bandwidth (for the clamping force) for the final comparison in terms of energy and responsiveness metrics. The chosen control parameters mentioned here (such as ω_n and ξ) will remain the same over the course of all optimizations. This is performed to have fixed control design for the optimization procedure, and the only change will be the physical parameters of the system. These physical parameters and their values and their range are mentioned in Table 6.1. For the EHB, they include cylinder's volume (V_{cyl}), cross-sectional area of the build valve when fully open (S_b), cylinder's cross-section surface (S_p), brake pad's mass (m_p) and caliper stiffness (K_{cal}). For EMB, they include inductance of the electric motor (L_m), electrical resistance (R_m), total moment of inertia (J_m), axial viscous friction (D_m), planetary gear reduction ratio (N_s), ball-screw gear reduction ratio (N_p), caliper stiffness K_{cal}, and electromotive force constant (K_t). For the EWB, these parameters include the same as EMB actuator in addition to wedge angle (α) and wedge mass (m_w). Figure 6.1 shows the Bode magnitude plots of T, S, and Y for this type of control design. The transfer functions and controller models defined above are mathematically expressed as follows. Note that G_{p_I} is the transfer function for the current plant, G_{p_ω} is the transfer function for the angular velocity plant and G_{p_F} is the transfer function for the force plant.

$$G_{p_I} = \frac{N^{G_{p_I}}}{D^{G_{p_I}}}, \tag{6.1}$$

where $N^{G_{p_I}} := J_m s^2 + D_m s + (N_s N_p)^2 K_{cal}$ and
$D^{G_{p_I}} := (L_m J_m) \cdot s^3 + (R_m J_m + L_m D_m) \cdot s^2 + (R_m D_m + L_m (N_s N_p)^2 K_{cal} + K_t^2) \cdot s + R_m (N_s N_p)^2 K_{cal}$,

$$Y_1 = \frac{1}{G_{p_I}} \times \frac{\omega_{n_1}^2}{s^2 + 2 \times \xi \times \omega_{n_1} \times s + \omega_{n_1}^2}, T_1 = \frac{\omega_{n_1}^2}{s^2 + 2 \times \xi \times \omega_n \times s + \omega_{n_1}^2}, \tag{6.2}$$

$$G_{p_\omega} = \frac{K_t \times s}{J_m s^2 + D_m s + (N_s N_p)^2 K_{cal}} \tag{6.3}$$

$$G_{p_2} = T_1 \times G_{p_\omega} = \frac{\omega_{n_1}^2}{s^2 + 2 \times \xi \times \omega_n \times s + \omega_{n_1}^2} \times \frac{K_t \times s}{J_m s^2 + D_m s + (N_s N_p)^2 K_{cal}}, \tag{6.4}$$

$$G'_{p_2} = \frac{G_{p_2}}{s} \tag{6.5}$$

$$Y_2 = \frac{1}{G'_{p_2}} \times \frac{\omega_{n_2}^2}{s^2 + 2 \times \xi \times \omega_{n_2} \times s + \omega_{n_2}^2} \times \frac{1}{s + W_1} \times (\frac{W_2}{s + W_2})^2, \qquad (6.6a)$$

$$T_2 = \frac{\omega_{n_2}^2}{s^2 + 2 \times \xi \times \omega_{n_2} \times s + \omega_{n_2}^2} \times \frac{s}{s + W_1} \times (\frac{W_2}{s + W_2})^2, \qquad (6.6b)$$

$$G_{p_F} = \frac{K_{cal} N_s N_p}{s} \qquad (6.7)$$

$$G_{p_3} = T_2 \times G_{p_F} = \frac{\omega_{n_2}^2}{s^2 + 2 \times \xi \times \omega_{n_2} \times s + \omega_{n_2}^2} \times \frac{s}{s + W_1} \times (\frac{W_2}{s + W_2})^2 \times \frac{K_{cal} N_s N_p}{s}, \quad (6.8)$$

$$Y_3 = \frac{1}{G_{p_3}} \times \frac{\omega_{n_3}^2}{s^2 + 2 \times \xi \times \omega_{n_3} \times s + \omega_{n_3}^2} \times (\frac{W_3}{s + W_3})^4, \qquad (6.9a)$$

$$T_3 = \frac{\omega_{n_3}^2}{s^2 + 2 \times \xi \times \omega_{n_3} \times s + \omega_{n_3}^2} \times (\frac{W_3}{s + W_3})^4, \qquad (6.9b)$$
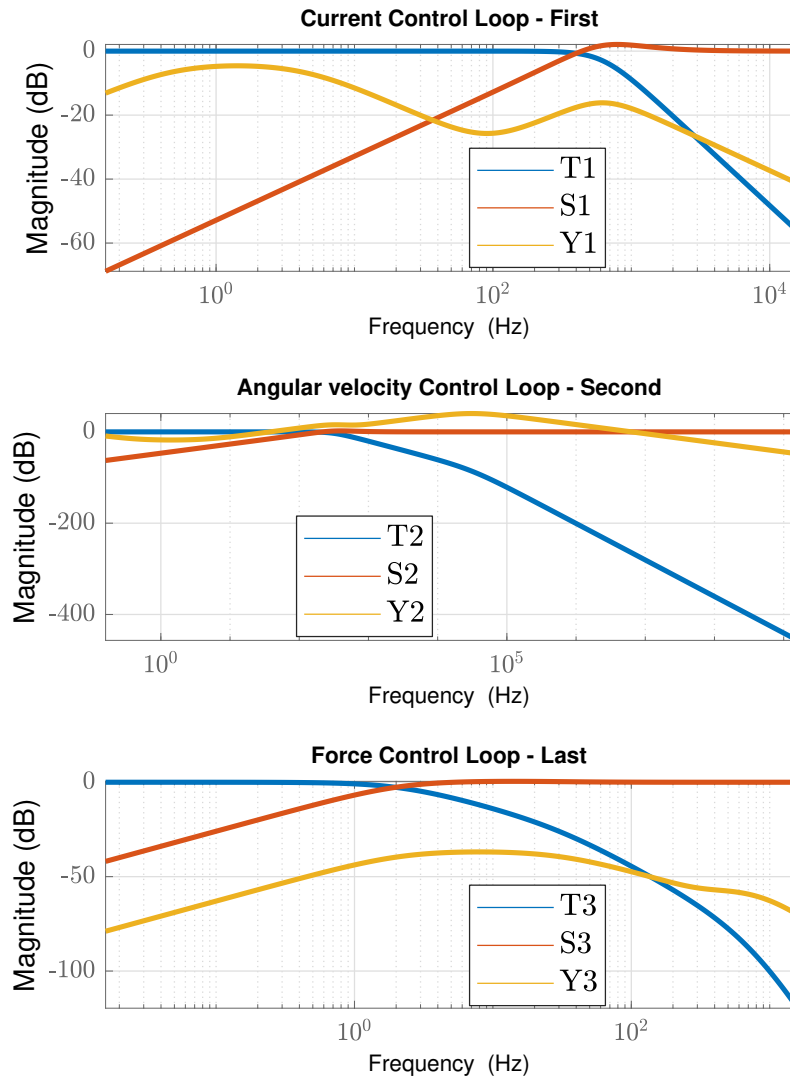
Figure 6.1: An example design of cascaded controllers for the EMB/EWB.

After designing the controllers, we then utilized the aforementioned transfer functions to optimize actuator response and actuator usage. The process of optimization starts with designing the controllers based on the physical parameters of the system and deriving these transfer functions as a function of the physical system parameters (since the parameters change, the plant transfer functions (G_p) change, and therefore, these transfer functions will be different for each set of physical parameters).

The bandwidth of a plant is related to its dynamic response, and therefore, increasing the bandwidth would result in faster system response. The bandwidth of a system/plant is

defined as the frequency range where the magnitude of the system gain does not drop below -3 dB. For EMB/EWB, the plant transfer function, which is chosen (denoted as G_p here) for calculating the system bandwidth, is from voltage input to the clamping force output. For EHB, the plant transfer function maps u_b to the clamping force. The bandwidth of the plant for all these actuators is denoted as $Bandwidth\{G_p\}$.

Another factor to consider is the actuator's power usage which is related to the actuator's effort, and hence, it is related to the Youla transfer function, denoted as $Y(s)$. The Youla transfer function for the overall system in case of cascaded control design would become $Y_{sys} = Y_1 \times Y_2 \times Y_3$. Y_{sys} stands for the Youla transfer function from the clamping force reference to the voltage input (or to the u_b for the EHB), which is the Youla transfer function of the overall control system. It can be shown if the magnitude of $T_y(s)$ or the gain of closed-loop transfer function is one at low frequencies, the Youla transfer function at low frequencies is inversely related to the plant transfer function $G_p(s)$ (From Equation (5.1), if $T_y = 1$, then $Y = \frac{1}{G_p}$). By increasing the plant gain at low frequency (approximately its DC gain, denoted as $DC\{G_p\}$ in this section), $Y(s)$ will decrease at low frequencies.

Furthermore, we need to lower the overall values of the Youla transfer function magnitude at other important frequencies, especially around the plant bandwidth. This will ensure the reduction of the actuator effort in all possible frequencies. To this end, we can use an H2 norm of this transfer function. H2 norm is related to the output signal energy when the system input is an impulse [67]. Since we are interested in a specific frequency range of the Youla transfer function, a band-pass filter, see Figure 6.2, is used to emphasize the frequency region of interest. ω_L and ω_H are chosen to be $0.1 \times Bandwidth\{G_p\}$ and $1e4 \times Bandwidth\{G_p\}$. The large range is chosen specifically to account for low and high frequency range of Youla transfer function around the bandwidth. This will ensure that the Youla transfer function magnitudes at low and mid-range frequencies stay low. The optimization problem is then formulated by combining all these costs as given in Equation (6.10):

$$\underset{x}{\text{minimize}} \quad f(x) = \alpha_1 \times ||Y_{sys} \times W_Y||_2 + \alpha_2 \times \frac{1}{DC\{G_p\}} + \alpha_3 \times \frac{1}{\text{Bandwidth}\{G_p\}} \quad (6.10)$$

$$\text{subject to} \quad x \in [x_{\min}, x_{\max}],$$

where α_1, α_2, and α_3 are tuning parameters, and x is the vector of physical parameters of the system that can be changed during the design process (e.g., gear ratios, moments of inertia, and motor's inductance). x_{min} and x_{max} denote the minimum and maximum of the parameter set, respectively (refer to Table 6.1 for the range of parameters and their initial values). W_Y is the frequency weighting function for H_2 norm optimization. It should be noted that each cost in Equation (6.10) is normalized by its nominal value to ensure the minimization of the three costs is done without bias. A choice of physical parameters for each actuator, their initial and optimized value are given in Table 6.1. We can solve Equation 6.10 using a nonlinear solver since the cost includes nonlinear components. We have used interior point algorithm (in fmincon function of MATLAB) to solve this problem.
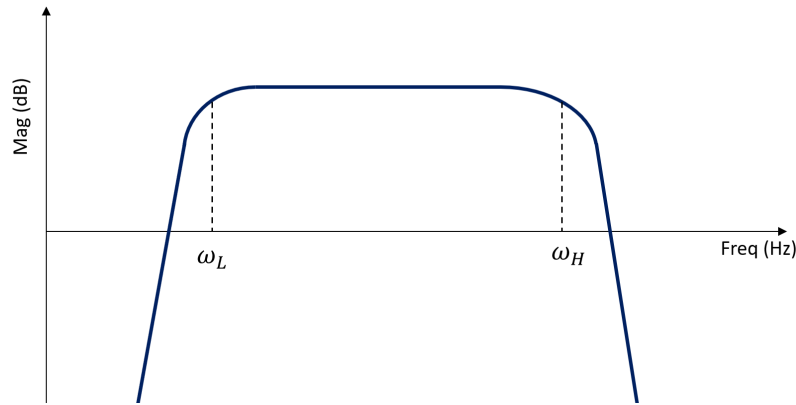
Figure 6.2: Band-pass filter, W_Y, is used to emphasize specific frequency region of Youla transfer function in the H_2 norm optimization.

The nonlinear optimization case in the next section is also solved using the same solver.

6.2 Nonlinear Optimization

Using linear transfer functions to optimize the plants provide us with an optimized initial parameter set. Although this set might be good enough for primarily linear plants; most brake actuators are nonlinear due to different factors such as friction, plant saturation, and dead-zone. Therefore, to further optimize the plants, we should perform optimization with the nonlinear plants to consider all the nonlinear effects. Since all the plants are going to run in the feedback control environment in practice, the nonlinear optimization is done on the closed-loop systems. A 10 kN step clamp force reference target is chosen for the brake's closed-loop system. This 10 kN step reference is chosen as a way to benchmark the performance of the actuators and their controllers. The controllers are designed in the same way explained in chapter 5 and 6.1. The control parameters are fixed in the same way as the transfer function optimization while the physical parameters of the systems change. Since the physical parameters of the system are changed, we need to recalculate the controllers at each step of function evaluation in the optimization (G_p changes, and so does Y and G_c). Since the optimization is performed on nonlinear plants, a different objective function should be used. The objective function for the nonlinear optimization consists of four parts: energy usage, maximum power, settling time, and overshoot percentage. Energy usage (E_{usage}) is the total amount of energy used by the actuator to follow the target in two seconds (enough for the actuators to reach and hold the target). Maximum power ($\max \mathbb{P}_{usage}$) is the maximum power used by the actuator during the 2 seconds that the actuator follows the 10 kN step reference. Settling time (T_s) is the time that it takes for the caliper force to build up to near $\pm 2\%$ of the steady-state value. Overshoot percentage

($OS\%$) is the percentage that the maximum value of the caliper force deviates from the 10 kN reference target. Power usage for the EMB and EWB is defined as current multiplied by the voltage. For the EHB, we are adding up the amount of power loss (denoted as $\mathbb{P}_{build}$ and $\mathbb{P}_{dump}$) to be equal to the power usage (Figure 4.1b):

$$\mathbb{P}_{build} = e_{build} \times f_{build} = (P_{in} - \frac{\beta_{hf}}{V_{Cyl}} \times q_{cyl}) \times \{C_d S_b u_b \sqrt{\frac{2}{\rho}(P_{in} - \frac{\beta_{hf}}{V_{cyl}} q_{cyl})}\} \qquad (6.11a)$$

$$\mathbb{P}_{dump} = e_{dump} \times f_{dump} = (\frac{\beta_{hf}}{V_{Cyl}} \times q_{cyl}) \times \{C_d S_d u_d \sqrt{\frac{2}{\rho}(\frac{\beta_{hf}}{V_{cyl}} q_{cyl})}\} \qquad (6.11b)$$

Taking all of these into account, the cost function for nonlinear optimization is given in Equation 6.12. Note that each cost is normalized by its nominal value.

$$\begin{aligned} \underset{x}{\text{minimize}} \quad & f(x) = \alpha_1 \times E_{usage} + \alpha_2 \times \max \mathbb{P}_{usage} + \alpha_3 \times T_s + \alpha_4 \times OS\% \\ \text{subject to} \quad & x \in [x_{min}, x_{max}] \end{aligned} \qquad (6.12)$$

Table 6.1: Initial and optimized physical parameter values of EMB, EWB and EHB and the range of the parameters.

	Parameter	Units	Lower Bound	Upper Bound	Initial	TF-based Opt.	Nonlinear Opt.
EMB	L_m	H	$4.48{\times}10^{-5}$	$5{\times}10^{-3}$	$5.6{\times}10^{-5}$	$6.36{\times}10^{-5}$	$2.8{\times}10^{-3}$
	R_m	Ω	$2.50{\times}10^{-2}$	$1{\times}10^{-1}$	$5{\times}10^{-2}$	$2.5{\times}10^{-2}$	$3.76{\times}10^{-2}$
	J_m	$\mathrm{kg\,m^2\,s^{-2}}$	$6.0{\times}10^{-5}$	$5.8{\times}10^{-4}$	$2.9{\times}10^{-4}$	$7.19{\times}10^{-5}$	$1.03{\times}10^{-4}$
	D_m	$\mathrm{N\,m\,s}$	$2.0{\times}10^{-4}$	$1.5{\times}10^{-2}$	$9{\times}10^{-3}$	$2.02{\times}10^{-4}$	$9.0{\times}10^{-4}$
	N_s	-	$7.96{\times}10^{-5}$	$1.3{\times}10^{-3}$	$6.37{\times}10^{-4}$	$1.3{\times}10^{-3}$	$1.2{\times}10^{-3}$
	N_p	-	6/266	18/266	$4.14{\times}10^{-2}$	$6.74{\times}10^{-2}$	$6.26{\times}10^{-2}$
	K_{cal}	$\mathrm{N\,m^{-1}}$	$2.3{\times}10^{7}$	$4.3{\times}10^{7}$	$3.35{\times}10^{7}$	$4.3{\times}10^{7}$	$4.19{\times}10^{7}$
	K_t	$\mathrm{N\,m\,A^{-1}}$	$5.0{\times}10^{-2}$	$5.2{\times}10^{-1}$	$6.97{\times}10^{-2}$	$1.59{\times}10^{-1}$	$4.3{\times}10^{-1}$
EWB	L_m	H	$4.48{\times}10^{-5}$	$5{\times}10^{-3}$	$5.6{\times}10^{-5}$	$4.7{\times}10^{-3}$	$4.48{\times}10^{-5}$
	R_m	Ω	$2.50{\times}10^{-2}$	$1{\times}10^{-1}$	$5{\times}10^{-2}$	$2.5{\times}10^{-2}$	$2.6{\times}10^{-2}$
	J_m	$\mathrm{kg\,m^2\,s^{-2}}$	$6.0{\times}10^{-5}$	$5.8{\times}10^{-4}$	$2.9{\times}10^{-4}$	$5.8{\times}10^{-4}$	$9.26{\times}10^{-5}$
	D_m	$\mathrm{N\,m\,s}$	$2.0{\times}10^{-4}$	$1.5{\times}10^{-2}$	$9{\times}10^{-3}$	$2.0{\times}10^{-4}$	$2.1{\times}10^{-4}$
	N_s	-	$7.96{\times}10^{-5}$	$7.96{\times}10^{-4}$	$4.77{\times}10^{-4}$	$7.96{\times}10^{-4}$	$7.89{\times}10^{-4}$
	N_p	-	6/266	18/266	$4.17{\times}10^{-2}$	$6.77{\times}10^{-2}$	$6.76{\times}10^{-2}$
	K_{cal}	$\mathrm{N\,m^{-1}}$	$2.3{\times}10^{7}$	$4.3{\times}10^{7}$	$3.35{\times}10^{7}$	$4.3{\times}10^{7}$	$4.29{\times}10^{7}$
	K_t	$\mathrm{N\,m\,A^{-1}}$	$5.0{\times}10^{-2}$	$5.2{\times}10^{-1}$	$6.97{\times}10^{-2}$	$5.0{\times}10^{-2}$	$5.88{\times}10^{-2}$
	α	degrees	10	24.5	10	24.5	24
	m_w	kg	0.1	0.5	0.3	$2.9{\times}10^{-1}$	$3.15{\times}10^{-1}$
EHB	V_{cyl}	$\mathrm{m^3}$	$1.6{\times}10^{-5}$	$1.28{\times}10^{-4}$	$1.6{\times}10^{-5}$	$1.6{\times}10^{-5}$	$7.93{\times}10^{-5}$
	S_b	$\mathrm{m^2}$	$1{\times}10^{-7}$	$4{\times}10^{-7}$	$4.0{\times}10^{-7}$	$4.0{\times}10^{-7}$	$2.16{\times}10^{-7}$
	S_p	$\mathrm{m^2}$	$6.38{\times}10^{-4}$	$1.02{\times}10^{-2}$	$1.6{\times}10^{-3}$	$1.7{\times}10^{-3}$	$3.7{\times}10^{-3}$
	m_p	kg	$5{\times}10^{-1}$	2	1.973	1.967	1.25
	K_{cal}	$\mathrm{N\,m^{-1}}$	$2.3{\times}10^{7}$	$4.3{\times}10^{7}$	$4.3{\times}10^{7}$	$4.3{\times}10^{7}$	$3.69{\times}10^{7}$

Simulation Results and Discussion

7.1 Actuator optimization

Figures 7.1–7.3 show the results of a 10 kN clamp force step response and the linear and non-linear optimization of brake-by-wire actuators. These simulations are performed using the nonlinear plant of the actuators. The nonlinearities that exist in the EMB and EWB include motor current and voltage saturation, brake caliper saturation, and the Lugre friction model. The nonlinearities in the EHB include the valve nonlinearities and the dead-zone. The "Initial" represents the initial set of parameters of the plant before the optimization. The initial setting for each actuator is compared with a similar setting in the literature to make sure the results are sound and follow other researchers' results. However, for the optimized plants' results, since this is the first study that discusses optimization on these physical parameters, there are no other papers to compare the results with. The "TF-based Opt." represents the linear transfer function optimization, and "Nonlinear Opt." represents the results for the set of plant parameters after the optimization is performed using the nonlinear plants as discussed in Section 6.2.

For the EHB, Figure 7.1 shows that the transfer function-based and the nonlinear optimization both have reduced the cylinder pressure. It must be noted that the results for the initial set of parameters are consistent with [64]. The cylinder's pressure in the Zhao et al. reaches steady-state around 0.3 seconds, similar to the results for this study. This shows that robust control along with the linearization is working for this EHB actuator. The readers have to note that the difference between the EHB model studied here is that the valves are considered to change continuously, and therefore, a continuous Youla control scheme is used to control the valves; however, in reality, this needs to be taken care of using a digital controller and pulse width modulation technique. The clamping force response time for the optimized simulation has also decreased from 0.5 seconds to around 0.3 seconds and 0.2 seconds for TF-based and nonlinear optimization, respectively. The power usage plot shows that, in all the cases, the power consumption stops once the actuators reach the steady-state target. This is because of the switching logic that closes both valves once they reach the steady-state value of the clamping force. Since the optimized plants reach the steady-state faster, and they use less actuation to do so, their energy and power usage is

Table 7.1: Comparison of the amount of energy used in the 10 kN step response for 2 seconds (the amounts are in Joules).

	EMB	EWB	EHB
Initial set	15.5	60.13	109.73
TF-Based optimized set	2.73	1.91	44.36
Nonlinear optimized set	1.69	2.14	29.70

reduced (see Table 7.1).

Figure 7.1: Comparison of the initial parameter sets vs. optimized in an EHB for a 10 kN step input. The clamp force plot for the initial parameter setting was consistent with Zhao et al. [64].

For the EMB, Figure 7.2 illustrates that the clamping force step response is about the same for all plants. This is because the controllers are set to have the same bandwidth; they all have the same response. In this case, the nonlinearities are mitigated by robust controllers, and the current/voltage saturation is taken care of by the anti-windup compensator. As shown, the current reaches its saturation level for the initial EMB plant, and the gain anti-windup is shown to be working. However, the difference between the plants manifests itself in the power consumption plot. The initial plant uses a lot more power and energy to perform the same task as the optimized plants. Tf-based and nonlinear optimized plants both have a significantly smaller power usage, with the nonlinear optimized plant consuming a slightly lower amount of power. The overall energy consumption for these plants is summarized in Table 7.1. Comparing to Line et al., for the initial parameter setting, the clamping force also reaches the steady-state around 0.2 seconds [6]. The current is higher than the results shown in Line et al.; however, the voltage is not plotted for their results. One explanation

is that a higher amount of current would result in lower voltage and vice versa. Another point to note on the power plot is the small oscillations on the Tf-based and nonlinear optimization parameter sets. This is due to the optimization bringing down the damping in the electrical components which resulted in small oscillations in the voltage and therefore power. This could be mitigated by manually changing the Youla controller second order damping factor (ξ in second order Youla filters) but it is left to show the original results of the optimization without hand tuning.
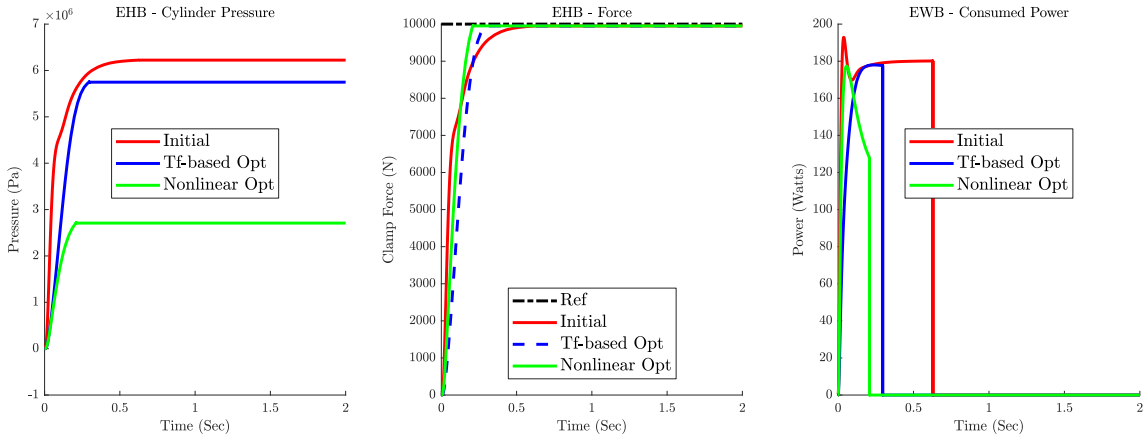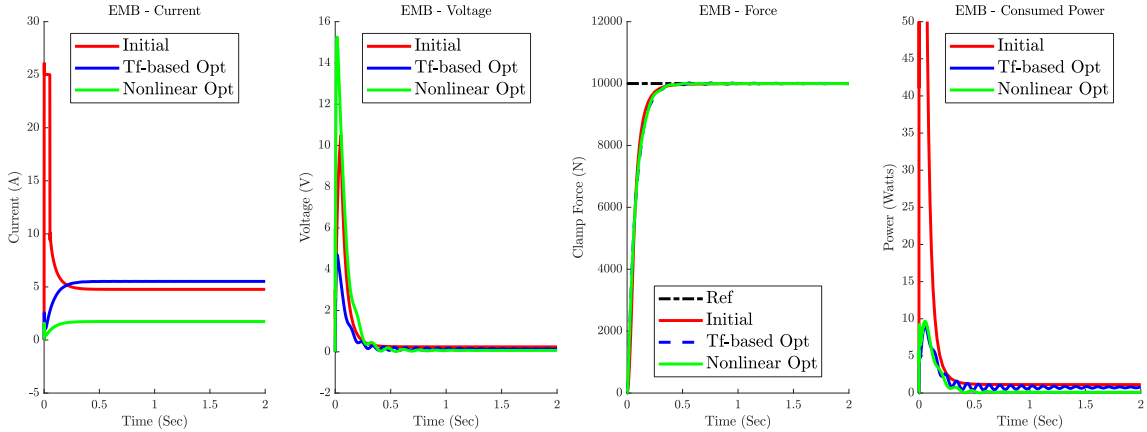

Figure 7.2: Comparison of the initial parameter sets vs. optimized in an EMB for a 10 kN step input. The clamp force plot for the initial parameter setting was consistent with Line et al. [6]

For the EWB, Figure 7.3 shows the step response for all the plants. For the initial parameter setting, the clamping force reaches to steady-state in around 0.5 seconds. Compared to Che Hasan et al., which uses a PID controller, this is around 0.2 seconds faster [12]. Additionally, using the Youla parameterization along with cascaded control, the overshoot is also smaller. The voltage peak for both are around the same, although the voltage for this paper is slightly higher. The nonlinear optimized plant is showing a faster response than the transfer function optimized and the initial plant. The overshoot in the nonlinear optimization of the plant has also slightly decreased when compared with the Tf-based optimization plant. As shown, the current once again saturates for the initial plant. For this plant, the current was saturated for around 0.3 seconds, and the anti-windup compensation has taken care of this; however, this has negatively impacted the closed-loop response and made it slower. Looking at the power consumption, it is clear that the Tf-based opt. has used a slightly lower amount of power, and the nonlinear opt. has used a significantly lower amount of actuation power. It should be noted that the voltage and current go to negative overshoots in all the plants, which comes from the fact that the clamping force overshoots and it needs to go back to target levels after that which results in negative values of current and voltage,

58

as shown in Figure 7.3.

One important point to note on the initial parameter setting in Table 7.1 is comparing the energy usage of different actuators. This shows a big discrepancy between EMB/EWB vs. EHB. One explanation for that could be the hydraulic pressure needs specific amount of energy to build up; however, when utilizing electro-mechanical brakes, it is all electric motors and mechanical components, there is no need for energizing any hydraulic circuits. There is only friction component that the motor has to overcome to reach to the clamping force. This results in a more efficient system.
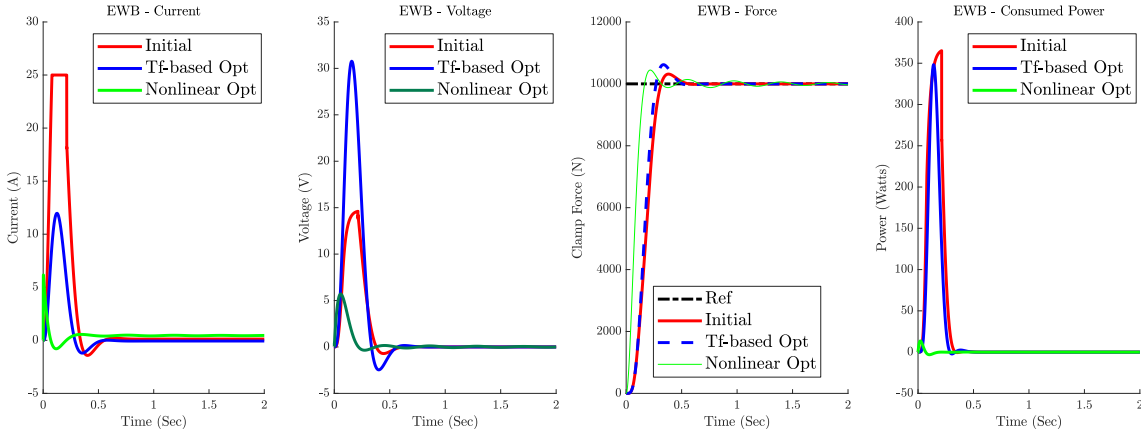
Figure 7.3: Comparison of the initial parameter sets vs. optimized in an EWB for a 10 kN step input. The clamp force plot for the initial parameter setting was consistent with Che Hassan et al. [12].

Similar to the step response, we have performed a ramp response of 10 kN/s with the saturation of 10 kN for the given plants. Figures 7.4–7.6 show similar results to the ones of the step response as discussed previously. It should be noted that the ramp response is only discussed in this thesis, and the cited papers above did not mention performing this test on the actuators.
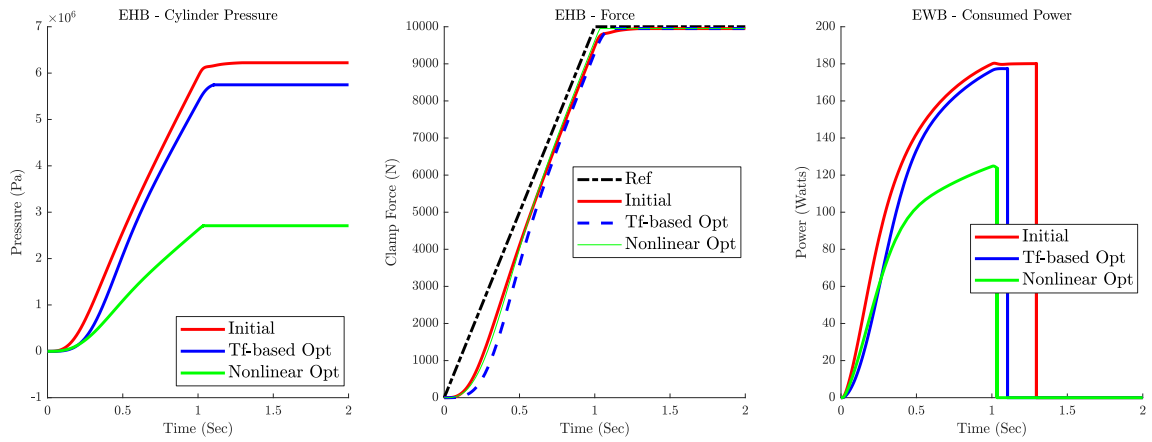
Figure 7.4: Comparison of the initial parameter sets vs. optimized in an EHB for a ramp input.
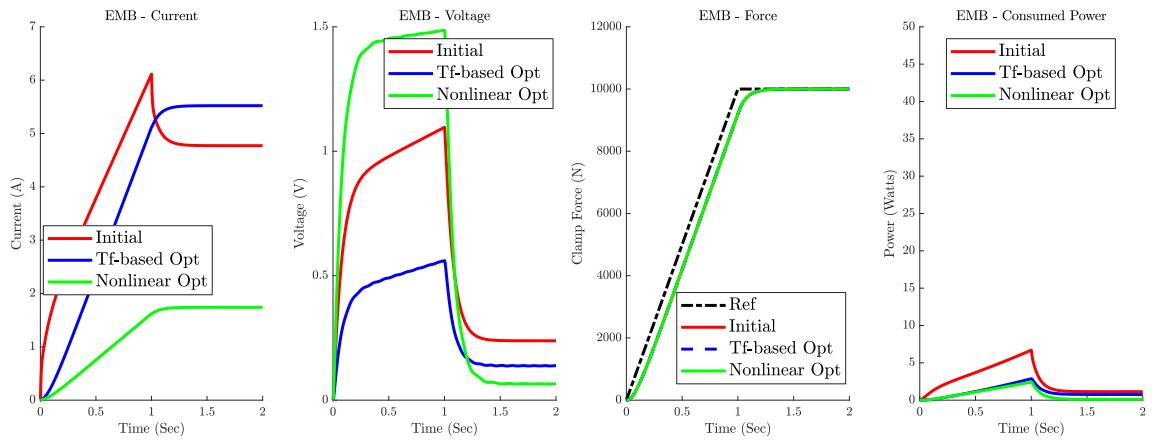
Figure 7.5: Comparison of the initial parameter sets vs. optimized in an EMB for a ramp input.
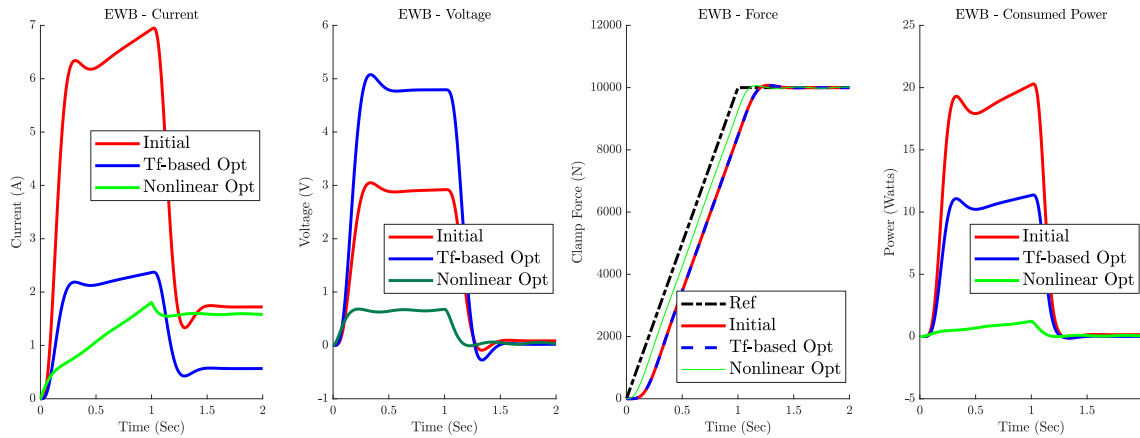
Figure 7.6: Comparison of the initial parameter sets vs. optimized in an EWB for a ramp input.

Table 7.2 shows the amount of energy usage by each plant with a different set of parameters. Comparing the energy usage of brake-by-wire actuators in Tables 7.1 and 7.2, we can conclude that EMB and EWB use significantly lower amounts of energy. However, looking once again at the Figures 7.1–7.3, we can see that EHB has at least a 0.1–0.2 seconds faster response than the dry brake-by-wire actuators such as EMB and EWB [80].

Table 7.2: Comparison of the amount of energy used in the ramp response for 2 seconds (the amounts are in Joules).

	EMB	EWB	EHB
Initial set	5.14	18.06	174.42
TF-Based optimized set	2.17	0.83	128.67
Nonlinear optimized set	1.41	0.82	89.72

7.2 straight-line braking maneuver

To compare the brakes and their topologies, straight-line braking is done with a 40 m/s initial speed on asphalt. The total mass of this vehicle is 2057.8 kg and the moment of inertia around y-axis is 3515 $kg \cdot m^2$. The ideal deceleration is set to be 0.8g for this maneuver. The topologies chosen for this comparison are the ones from the literature review explained in the first chapter. This includes 1. Front EHB and rear EMB, 2. All EWB, 3. Front EHB and rear EWB, 4. All EHB, and 5. All EMB. For each topology, there are three metrics being used as a comparison: stopping distance, stopping time, the energy usage of the front and rear actuators, and total energy expenditure of all the brake actuators during

the straight-line braking maneuver. This maneuver is done in a way that the ABS does not need to engage since as we will see in the Figure 7.8 the values of longitudinal slip remain low. If the maneuver was done on close to ABS condition, we would see longitudinal slip close to the maximum and near locking up. In those scenarios, the ABS has to be engaged to ensure the vehicle stops in the shortest distances and the wheels don't lock up.

Since all the brake topologies respond in a very similar manner in terms of vehicle dynamics, we first show how the vehicle would react in a straight-line braking event using the architecture explained in Chapter 5. Figure 7.8 shows longitudinal slips (s_x) for each tire. The negative values mean that the tires are in braking. As shown, the front and rear tires both reach specific longitudinal slip values and the rear tires have higher slip values than the front tires.
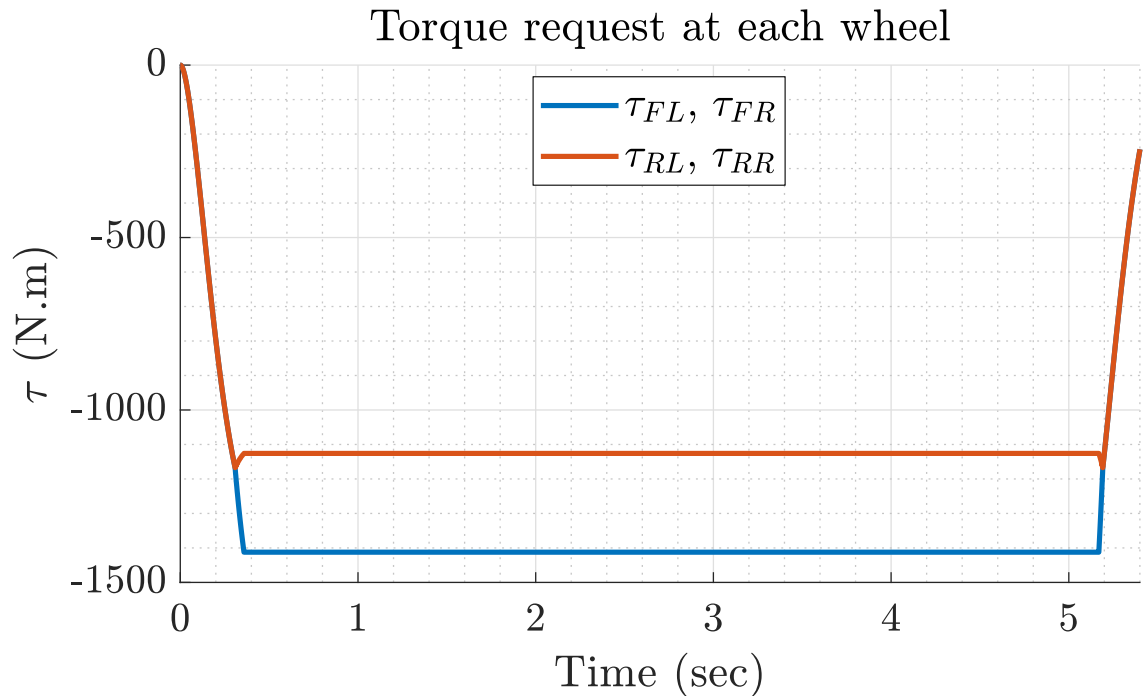
Figure 7.7: Brake torque allocated at each wheel during the straight-line braking maneuver
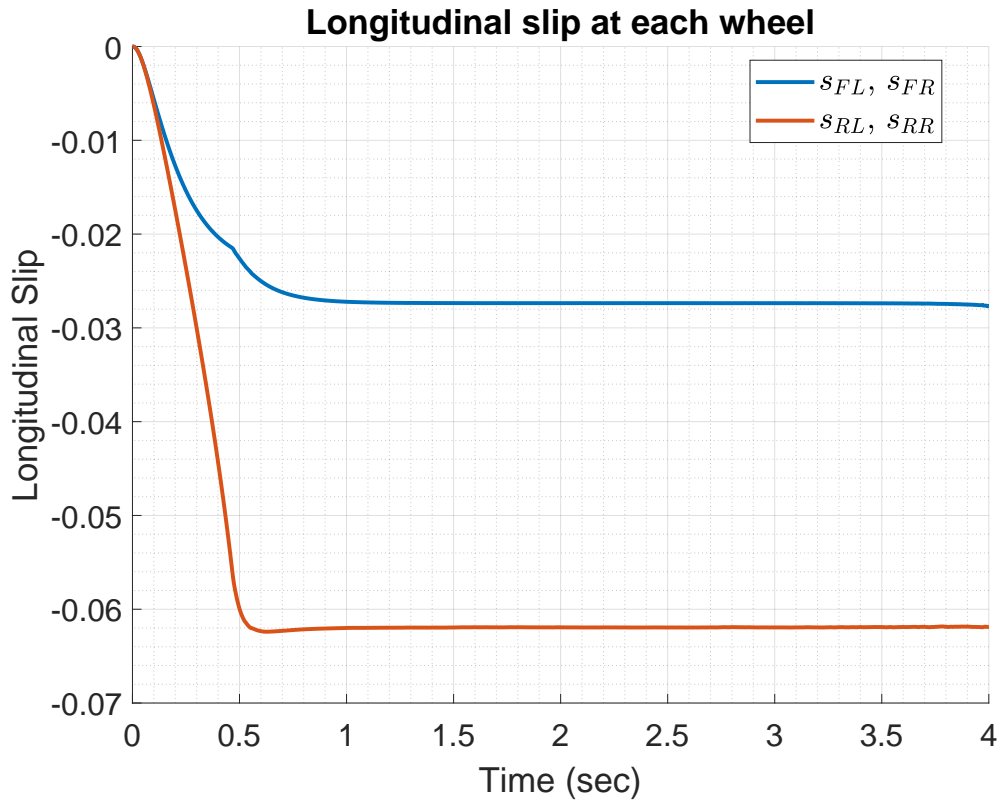
Figure 7.8: Longitudinal slip for each wheel
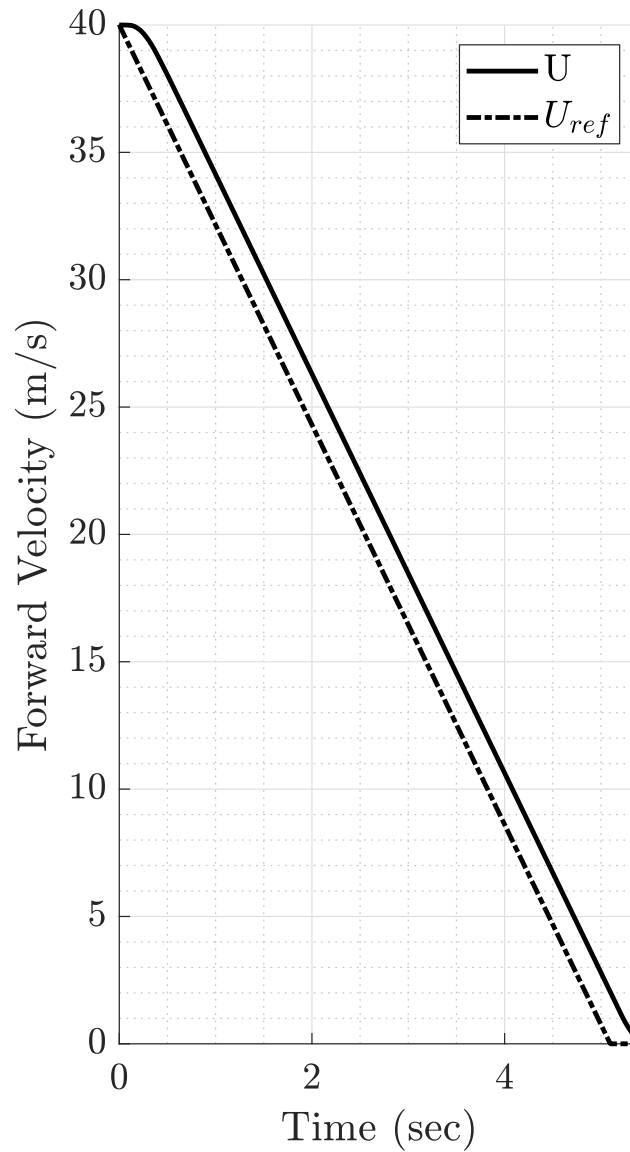
Figure 7.9: Longitudinal velocity of the vehicle

Figure 7.7 shows the brake torque request for this maneuver. This is the result of the control allocation block. The right and left tires have the same brake torque request as they are both on the same surface. The brake force distribution during the straight-line braking is dependant on deceleration. Since the deceleration would increase the normal forces on the front and decrease them on the rear. Therefore, there is more braking force available on the front tires than the rear ones. The rear tires would require lower torque as there is lower

normal force and therefore lower maximum torque available in the rear tires. However, the longitudinal slip of the rear wheels are larger than the front wheels despite of the availability of lower maximum torque. In the following subsections, we will go over the results for each brake topology for this specific maneuver.

7.2.1 Front EHB + Rear EMB

Table 7.3 shows the result of straight-line braking for the front EHB and rear EMB topology with and without optimization. As it is shown, the optimization has slightly reduced the stopping time and stopping distance; however, this reduction seems to be small. The most of reduction is in the energy usage as excepted with nonlinear optimization parameter set using around 1/3rd of the initial energy.

Table 7.3: Front EHB+Rear EMB topology energy usage, stopping time and distance during straight-line braking for different parameter sets

	Stopping Time (s)	Stopping Distance (m)	Energy-Front (J)	Energy-Rear (J)	Energy-Total (J)
Initial set	5.41	112.15	359.05	41.67	400.72
TF-Based Optimization	5.40	112.49	192.36	126.8	319.17
Nonlinear Optimization	5.38	112.02	126.24	6.00	132.25

7.2.2 All EWB

Similar to the previous topology, an all-EWB topology also benefits heavily in terms the energy usage with the nonlinear optimization reducing the energy usage. However, this energy reduction seems to be a lot more (1/100th of the initial set). This is due to the fact that the power consumption especially at steady state has significantly reduced with the new parameter setting. Additionally, we see this optimization also effect stopping distance by 10.45 m which is 8% reduction of the initial setting stopping distance. The stopping time also has reduced slightly by 0.23 seconds.

Table 7.4: All EWB topology energy usage, stopping time, and distance during straight-line braking for different sets of parameters

	Stopping Time (s)	Stopping Distance (m)	Energy-Front (J)	Energy-Rear (J)	Energy-Total (J)
Initial set	5.60	122.26	551.44	418.22	969.66
TF-Based Optimization	5.41	114.67	8.91	5.96	14.877
Nonlinear Optimization	5.37	111.81	7.09	5.30	12.39

7.2.3 Front EHB + rear EWB

For the front EHB and rear EWB topology, the stopping distance reduces by around 3.97 m between the initial set and the nonlinear optimization parameter set. The stopping time also reduces by 0.1 second. However, the energy reduction seen in this topology is a lot more. This is due to the significant energy usage reduction of EWB actuators in the rear.

Table 7.5: Front EHB + rear EWB topology energy usage, stopping time and distance during straight-line braking for different sets of parameters

	Stopping Time (s)	Stopping Distance (m)	Energy-Front (J)	Energy-Rear (J)	Energy-Total (J)
Initial set	5.47	115.89	340.10	435.10	776.04
TF-Based Optimization	5.40	113.63	172.42	6.12	178.54
Nonlinear Optimization	5.37	111.92	124.53	5.45	129.98

7.2.4 All EHB

For an all EHB topology, there is not much difference between stopping distance and stopping time when the optimization is done. However, we again see a significant reduction in energy usage of brake actuators by around 1/3rd.

Table 7.6: All EHB topology energy usage, stopping time and distance during straight-line braking for different sets of parameters

	Stopping Time (s)	Stopping Distance (m)	Energy-Front (J)	Energy-Rear (J)	Energy-Total (J)
Initial set	5.42	112.22	363.82	324.25	688.06
TF-Based Optimization	5.40	112.88	183.14	162.33	345.47
Nonlinear Optimization	5.39	112.22	122.79	110.06	232.86

7.2.5 All EMB

For an all EMB topology, we can observe that stopping distance and time are around the same for all the parameter sets. And the energy usage has been reduced by around 6.7 times compared to the initial set.

Table 7.7: All EMB topology energy usage, stopping time and distance during straight-line braking for different sets of parameters

	Stopping Time (s)	Stopping Distance (m)	Energy-Front (J)	Energy-Rear (J)	Energy-Total (J)
Initial set	5.39	112.20	60.25	41.36	101.61
TF-Based Optimization	5.65	117.85	172.38	133.57	305.96
Nonlinear Optimization	5.39	112.20	9.23	5.99	15.21

7.2.6 Comparison of different topologies

In this subsection, we compare all the different topologies by their initial parameter sets and also when the nonlinear optimized parameters are used. Table 7.8 shows the performance of all the different topologies in their initial setting. We can see that an all-EMB topology has the second shortest stopping distance and the smallest stopping time while using the least amount of energy. The front EHB and rear EMB topology have around the same stopping time and a lower stopping distance. However, the energy usage for this topology is 4 times higher than an all-EMB topology.

Next, looking at Table 7.9 shows all the topologies after the nonlinear optimization is performed on the actuators. We can see a very uniform stopping distance and stopping time along all the topologies. However, the energy usage by the actuators still varies. In this case, an all-EWB topology uses the least amount of energy, followed by an all-EMB topology.

Table 7.8: Comparison of different topologies in terms of energy usage, stopping time, and distance during straight-line braking for the initial sets of parameters

	Stopping Time (s)	Stopping Distance (m)	Energy-Total (J)
Front EHB+Rear EMB	5.41	112.15	400.72
All EWB	5.60	122.26	969.66
Front EHB+Rear EWB	5.47	115.89	776.04
All EHB	5.42	112.22	688.06
All EMB	5.39	112.20	101.61

Table 7.9: Comparison of different topologies in terms of energy usage, stopping time, and distance during straight-line braking for the optimized sets of parameters (using nonlinear optimization method)

	Stopping Time (s)	Stopping Distance (m)	Energy-Total (J)
Front EHB+Rear EMB	5.38	112.02	132.25
All EWB	5.37	111.81	12.39
Front EHB+Rear EWB	5.37	111.92	129.98
All EHB	5.39	112.22	232.86
All EMB	5.39	112.20	15.21

7.3 Conclusion

In this thesis, we presented the modeling (using bond graph) and a new control strategy (Youla parameterization) for three different brake-by-wire actuators for straight braking. We used a modular control functional architecture that can be used for both autonomous and non-autonomous vehicles BBW actuator controls.

On the actuators low level controllers and physical parameters, we did two different types optimizations: 1. Using transfer functions for optimization. 2. Using nonlinear optimization on energy, power and overshoot percentage of the plant. The physical optimization of these plants using linear transfer functions, and nonlinear plants were discussed, and the results were presented. The optimized results show a promising energy reduction when compared with the nominal parameters. EHB's, EMB's, and EWB's energy consumption were reduced to around 10%, 3%, and 20% of their original parameter sets, respectively.

We also looked at 5 different common brake topologies used in the literature and compared them between different parameter sets on mainly three different metrics in straight-line braking: stopping distance, stopping time, and total energy. At the end, we also compared the topologies against each other. We concluded that most of the brakes do similar in their stopping distance and time while the total energy varies significantly and it's lower for topolgies that have EWB and EMB actuators compared to all EHB topology.

7.4 Future work

There a few ideas that would be worth considering for future research ideas. The proposed optimization method can be equivalently and effectively utilized for other brake-by-wire actuators to reduce their energy consumption while increasing their dynamic response. It should be noted that in practice, other criteria such as structural, electrical, and heat transfer measures should be added to the optimization method.This can result in more constraints for the optimization problem, which in turn will alter the final results. However, the optimization framework and the objectives will stay the same. Usually, having more constraints will result in a lesser deviation from the initial results. However, as shown in the results, the gains in energy consumption and dynamic responsiveness would be high enough that additional constraints could be considered without penalizing too much the final energy consumption and dynamic responsiveness.

To further investigate the capabilities and limits of the BBW and the proposed architecture a few more testing scenarios besides straight-line braking can be done. This would include braking while cornering, and braking on split mu conditions. This would test out the control allocation block specifically and also would show the effect of possible potentials of BBW in other driving scenarios.

Another research that could further be looked at is the integration of these smart BBW actuators with the regenerative braking and their effect on the overall control architecture and the vehicle dynamics. For example, looking at ABS events on low mu surfaces would be

a specific maneuver to show if the integrated ABS and other control modules are correctly working to keep the vehicle stable in that sitution.

Furthermore, an intriguing avenue for exploration lies in the seamless integration of the established control architecture and BBW actuators with the motion planning and motion control layer, as outlined in the functional architecture chapter. This integration opens the door to investigating collision avoidance scenarios for autonomous vehicles and understanding how BBW systems influence these situations. By delving into these scenarios, the intricate interplay between control systems and actuators could be unraveled, gaining insights into how BBW technology can meaningfully enhance collision avoidance strategies within the realm of autonomous driving.

Bibliography

[1] F. Lamnabhi-Lagarrigue, A. Annaswamy, S. Engell, *et al.*, "Systems & Control for the future of humanity, research agenda: Current and future roles, impact and grand challenges," en, *Annual Reviews in Control*, vol. 43, pp. 1–64, 2017, ISSN: 13675788. DOI: `10.1016/j.arcontrol.2017.04.001`. [Online]. Available: `https://linkinghub.elsevier.com/retrieve/pii/S1367578817300573` (visited on 04/23/2021).

[2] Y. Yuan, J. Zhang, Y. Li, and C. Lv, "Regenerative Brake-by-Wire System Development and Hardware-In-Loop Test for Autonomous Electrified Vehicle," en, Mar. 2017. DOI: `10.4271/2017-01-0401`. [Online]. Available: `https://www.sae.org/content/2017-01-0401/` (visited on 05/21/2019).

[3] P. Sinha, "Architectural design and reliability analysis of a fail-operational brake-by-wire system from ISO 26262 perspectives," en, *Reliability Engineering & System Safety*, vol. 96, no. 10, pp. 1349–1359, Oct. 2011, Number: 10, ISSN: 09518320. DOI: `10.1016/j.ress.2011.03.013`. [Online]. Available: `https://linkinghub.elsevier.com/retrieve/pii/S095183201100041X` (visited on 05/21/2019).

[4] B. D. Gombert, M. Schautt, and R. P. Roberts, "The Development of Alternative Brake Systems," en, in *Encyclopedia of Automotive Engineering*, D. Crolla, D. E. Foster, T. Kobayashi, and N. Vaughan, Eds., Chichester, UK: John Wiley & Sons, Ltd, Apr. 2014, pp. 1–11, ISBN: 9780470974025. DOI: `10.1002/9781118354179.auto025`. [Online]. Available: `http://doi.wiley.com/10.1002/9781118354179.auto025` (visited on 06/07/2019).

[5] J. S. Cheon, "Brake By Wire System Configuration and Functions using Front EWB (Electric Wedge Brake) and Rear EMB (Electro-Mechanical Brake) Actuators," en, Oct. 2010. DOI: `10.4271/2010-01-1708`. [Online]. Available: `https://www.sae.org/content/2010-01-1708/` (visited on 06/07/2019).

[6] C. Line, C. Manzie, and M. Good, "Electromechanical Brake Modeling and Control: From PI to MPC," en, *IEEE Transactions on Control Systems Technology*, vol. 16, no. 3, pp. 446–457, May 2008, Number: 3, ISSN: 1063-6536, 1558-0865. DOI: `10.1109/`

71

`TCST.2007.908200`. [Online]. Available: `http://ieeexplore.ieee.org/document/4475522/` (visited on 01/17/2019).

[7] C. Line, C. Manzie, and M. Good, "Robust Control of an automotive electromechanical brake," en, *IFAC Proceedings Volumes*, vol. 40, no. 10, pp. 579–586, 2007, Number: 10, ISSN: 14746670. DOI: `10.3182/20070820-3-US-2918.00078`. [Online]. Available: `https://linkinghub.elsevier.com/retrieve/pii/S1474667015319765` (visited on 01/17/2019).

[8] T. Sakamoto, K. Hirukawa, and T. Ohmae, "Cooperative control of full electric braking system with independently driven four wheels," en, in *9th IEEE International Workshop on Advanced Motion Control, 2006.*, Istanbul, Turkey: IEEE, 2006, pp. 602–606. DOI: `10.1109/AMC.2006.1631728`. [Online]. Available: `http://ieeexplore.ieee.org/document/1631728/` (visited on 04/11/2020).

[9] H. Hartmann, M. Schautt, A. Pascucci, and B. Gombert, "eBrake® - The Mechatronic Wedge Brake," en, Oct. 2002, pp. 2002–01–2582. DOI: `10.4271/2002-01-2582`. [Online]. Available: `https://www.sae.org/content/2002-01-2582/` (visited on 04/12/2020).

[10] J. Fox, R. Roberts, C. Baier-Welt, L. M. Ho, L. Lacraru, and B. Gombert, "Modeling and Control of a Single Motor Electronic Wedge Brake," en, Apr. 2007. DOI: `10.4271/2007-01-0866`. [Online]. Available: `https://www.sae.org/content/2007-01-0866/` (visited on 10/22/2019).

[11] K. Han, M. Kim, and K. Huh, "Modeling and control of an electronic wedge brake," en, *Proceedings of the Institution of Mechanical Engineers, Part C: Journal of Mechanical Engineering Science*, vol. 226, no. 10, pp. 2440–2455, Oct. 2012, Number: 10, ISSN: 0954-4062, 2041-2983. DOI: `10.1177/0954406211435584`. [Online]. Available: `http://journals.sagepub.com/doi/10.1177/0954406211435584` (visited on 10/22/2019).

[12] M. H. Che Hasan, M. Khair Hassan, F. Ahmad, and M. H. Marhaban, "Modelling and Design of Optimized Electronic Wedge Brake," en, in *2019 IEEE International Conference on Automatic Control and Intelligent Systems (I2CACIS)*, Selangor, Malaysia: IEEE, Jun. 2019, pp. 189–193, ISBN: 978-1-72810-784-4. DOI: `10.1109/I2CACIS.2019.8825045`. [Online]. Available: `https://ieeexplore.ieee.org/document/8825045/` (visited on 10/22/2019).

[13] J. S. Cheon, J. Kim, and J. Jeon, "New Brake By Wire Concept with Mechanical Backup," en, *SAE International Journal of Passenger Cars - Mechanical Systems*, vol. 5, no. 4, pp. 1194–1198, Sep. 2012, Number: 4, ISSN: 1946-4002. DOI: `10.4271/2012-01-1800`. [Online]. Available: `https://www.sae.org/content/2012-01-1800/` (visited on 11/17/2019).

[14] M. A. A. Emam, A. S. Emam, S. M. El-Demerdash, S. M. Shaban, and M. A. Mahmoud, "Performance of Automotive Self Reinforcement Brake System," en, *Journal Of Mechanical Engineering*, vol. 1, no. 1, p. 7, 2012, Number: 1.

[15] F. Ahmad, K. Hudha, S. Mazlan, H. Jamaluddin, V. Aparow, and M. M. Yunos, "Simulation and experimental investigation of vehicle braking system employing a fixed caliper based electronic wedge brake," en, *SIMULATION*, vol. 94, no. 4, pp. 327–340, Apr. 2018, Number: 4, ISSN: 0037-5497, 1741-3133. DOI: 10.1177/0037549717733805. [Online]. Available: http://journals.sagepub.com/doi/10.1177/0037549717733805 (visited on 06/07/2019).

[16] L. M. Ho, R. Roberts, H. Hartmann, and B. Gombert, "The Electronic Wedge Brake - EWB," en, Oct. 2006. DOI: 10.4271/2006-01-3196. [Online]. Available: https://www.sae.org/content/2006-01-3196/ (visited on 06/07/2019).

[17] M. H. Putz, "VE Mechatronic Brake: Development and Investigations of a Simple Electro Mechanical Brake," en, Oct. 2010. DOI: 10.4271/2010-01-1682. [Online]. Available: https://www.sae.org/content/2010-01-1682/ (visited on 06/07/2019).

[18] R. de Castro, F. Todeschini, R. E. Araújo, S. M. Savaresi, M. Corno, and D. Freitas, "Adaptive-robust friction compensation in a hybrid brake-by-wire actuator," en, *Proceedings of the Institution of Mechanical Engineers, Part I: Journal of Systems and Control Engineering*, vol. 228, no. 10, pp. 769–786, Nov. 2014, ISSN: 0959-6518, 2041-3041. DOI: 10.1177/0959651813507562. [Online]. Available: http://journals.sagepub.com/doi/10.1177/0959651813507562 (visited on 03/29/2021).

[19] X. Gong, W. Ge, J. Yan, Y. Zhang, and X. Gongye, "Review on the Development, Control Method and Application Prospect of Brake-by-Wire Actuator," en, *Actuators*, vol. 9, no. 1, p. 15, Mar. 2020, ISSN: 2076-0825. DOI: 10.3390/act9010015. [Online]. Available: https://www.mdpi.com/2076-0825/9/1/15 (visited on 03/25/2021).

[20] R. Büchler, "Future Brake Systems And Technologies – MK C1® – Continental's brake system for future vehicle concepts," en, in *7th International Munich Chassis Symposium 2016*, P. D. P. E. Pfeffer, Ed., Series Title: Proceedings, Wiesbaden: Springer Fachmedien Wiesbaden, 2017, pp. 717–723. DOI: 10.1007/978-3-658-14219-3_45. [Online]. Available: http://link.springer.com/10.1007/978-3-658-14219-3_45 (visited on 03/30/2021).

[21] X. Gong, S. Chang, L. Jiang, and X. Li, "Research on regenerative brake technology of electric vehicle based on direct-drive electric-hydraulic brake system," en, *International Journal of Vehicle Design*, vol. 70, no. 1, p. 1, 2016, ISSN: 0143-3369, 1741-5314. DOI: 10.1504/IJVD.2016.073697. [Online]. Available: http://www.inderscience.com/link.php?id=73697 (visited on 03/31/2021).

[22] J. Ko, S. Ko, H. Son, B. Yoo, J. Cheon, and H. Kim, "Development of Brake System and Regenerative Braking Cooperative Control Algorithm for Automatic-Transmission-Based Hybrid Electric Vehicles," *IEEE Transactions on Vehicular Technology*, vol. 64, no. 2, pp. 431–440, Feb. 2015, Conference Name: IEEE Transactions on Vehicular Technology, ISSN: 1939-9359. DOI: 10.1109/TVT.2014.2325056.

[23] R. Shankar, J. Marco, and F. Assadian, "The Novel Application of Optimization and Charge Blended Energy Management Control for Component Downsizing within a Plug-in Hybrid Electric Vehicle," en, *Energies*, vol. 5, no. 12, pp. 4892–4923, Nov. 2012, Number: 12, ISSN: 1996-1073. DOI: `10.3390/en5124892`. [Online]. Available: `http://www.mdpi.com/1996-1073/5/12/4892` (visited on 11/20/2019).

[24] M. Yao, J. Miao, S. Cao, S. Chen, and H. Chai, "The Structure Design and Optimization of Electromagnetic-Mechanical Wedge Brake System," en, *IEEE Access*, vol. 8, pp. 3996–4004, 2020, ISSN: 2169-3536. DOI: `10.1109/ACCESS.2019.2962559`. [Online]. Available: `https://ieeexplore.ieee.org/document/8943394/` (visited on 03/31/2021).

[25] Y. Kwon, J. Kim, J. S. Cheon, H.-i. Moon, and H. J. Chae, "Multi-Objective Optimization and Robust Design of Brake By Wire System Components," en, *SAE International Journal of Passenger Cars - Mechanical Systems*, vol. 6, no. 3, pp. 1465–1475, Sep. 2013, Number: 3, ISSN: 1946-4002. DOI: `10.4271/2013-01-2059`. [Online]. Available: `https://www.sae.org/content/2013-01-2059/` (visited on 11/17/2019).

[26] Z. Fengjiao and W. Minxiang, "Multi-objective optimization of the control strategy of electric vehicle electro-hydraulic composite braking system with genetic algorithm," en, *Advances in Mechanical Engineering*, vol. 7, no. 3, p. 168 781 401 456 849, Mar. 2015, Number: 3, ISSN: 1687-8140, 1687-8140. DOI: `10.1177/1687814014568491`. [Online]. Available: `http://journals.sagepub.com/doi/10.1177/1687814014568491` (visited on 11/18/2019).

[27] T. Hierlinger, T. Dirndorfer, and T. Neuhauser, "A Method for the Simulation-Based Parameter Optimization of Autonomous Emergency Braking Systems," en, 2017, p. 9. [Online]. Available: `https://trid.trb.org/view/1483876` (visited on 11/03/2021).

[28] N. A. Kelling and W. Heck, "The BRAKE Project - Centralized Versus Distributed Redundancy for Brake-by-Wire Systems," en, Mar. 2002. DOI: `10.4271/2002-01-0266`. [Online]. Available: `https://www.sae.org/content/2002-01-0266/` (visited on 06/07/2019).

[29] S. Anwar, "Anti-Lock Braking Control of a Hybrid Brake-By-Wire System," en, *Proceedings of the Institution of Mechanical Engineers, Part D: Journal of Automobile Engineering*, vol. 220, no. 8, pp. 1101–1117, Aug. 2006, ISSN: 0954-4070, 2041-2991. DOI: `10.1243/09544070D22704`. [Online]. Available: `http://journals.sagepub.com/doi/10.1243/09544070D22704` (visited on 04/07/2021).

[30] S. M. Savaresi and M. Tanelli, *Active Braking Control Systems Design for Vehicles*, en, ser. Advances in Industrial Control. London: Springer London, 2010. DOI: `10.1007/978-1-84996-350-3`. [Online]. Available: `http://link.springer.com/10.1007/978-1-84996-350-3` (visited on 04/08/2021).

[31] H. K. Khalil, *Nonlinear control*. Prentice Hall, 2015.

[32] A. Soltani and F. Assadian, "New Slip Control System Considering Actuator Dynamics," en, *SAE International Journal of Passenger Cars - Mechanical Systems*, vol. 8, no. 2, pp. 512–520, Apr. 2015, ISSN: 1946-4002. DOI: `10.4271/2015-01-0656`. [Online]. Available: `https://www.sae.org/content/2015-01-0656/` (visited on 05/25/2021).

[33] S. Khastgir and P. Warule, "Published on 9th-12th January Vehicle Converted into a Hybrid Vehicle 2013, SIAT, India," en, p. 8, 2013.

[34] W. Li, G. Tan, Y. Liu, *et al.*, "Regenerative braking system design for an energy recuperative eddy current retarder," en, in *2015 IEEE International Transportation Electrification Conference (ITEC)*, Chennai, India: IEEE, Aug. 2015, pp. 1–5, ISBN: 978-1-5090-1911-3. DOI: `10.1109/ITEC-India.2015.7386865`. [Online]. Available: `http://ieeexplore.ieee.org/document/7386865/` (visited on 01/24/2019).

[35] C. He, G. Wang, Z. Gong, Z. Xing, and D. Xu, "A Control Algorithm for the Novel Regenerative–Mechanical Coupled Brake System with by-Wire Based on Multidisciplinary Design Optimization for an Electric Vehicle," en, *Energies*, vol. 11, no. 9, p. 2322, Sep. 2018, Number: 9 Publisher: Multidisciplinary Digital Publishing Institute. DOI: `10.3390/en11092322`. [Online]. Available: `https://www.mdpi.com/1996-1073/11/9/2322` (visited on 04/07/2021).

[36] R. de Castro, R. E. Araújo, M. Tanelli, S. M. Savaresi, and D. Freitas, "Torque blending and wheel slip control in EVs with in-wheel motors," en, *Vehicle System Dynamics*, vol. 50, no. sup1, pp. 71–94, Jan. 2012, ISSN: 0042-3114, 1744-5159. DOI: `10.1080/00423114.2012.666357`. [Online]. Available: `http://www.tandfonline.com/doi/abs/10.1080/00423114.2012.666357` (visited on 04/01/2021).

[37] M. Ehsani, Ed., *Modern electric, hybrid electric, and fuel cell vehicles: fundamentals, theory, and design*, en, ser. Power electronics and applications series. Boca Raton: CRC Press, 2005, ISBN: 978-0-8493-3154-1.

[38] F. Sangtarash, V. Esfahanian, H. Nehzati, S. Haddadi, M. A. Bavanpour, and B. Haghpanah, "Effect of Different Regenerative Braking Strategies on Braking Performance and Fuel Economy in a Hybrid Electric Bus Employing CRUISE Vehicle Simulation," en, *SAE International Journal of Fuels and Lubricants*, vol. 1, no. 1, pp. 828–837, Jun. 2008, ISSN: 1946-3960. DOI: `10.4271/2008-01-1561`. [Online]. Available: `https://www.sae.org/content/2008-01-1561/` (visited on 05/27/2021).

[39] L. Zhang, L. Yu, Z. Wang, L. Zuo, and J. Song, "All-Wheel Braking Force Allocation During a Braking-in-Turn Maneuver for Vehicles With the Brake-by-Wire System Considering Braking Efficiency and Stability," *IEEE Transactions on Vehicular Technology*, vol. 65, no. 6, pp. 4752–4767, Jun. 2016, Conference Name: IEEE Transactions on Vehicular Technology, ISSN: 1939-9359. DOI: `10.1109/TVT.2015.2473162`.

Bibliography

[40]   S. Anwar, "Generalized predictive control of yaw dynamics of a hybrid brake-by-wire equipped vehicle," en, *Mechatronics*, vol. 15, no. 9, pp. 1089–1108, Nov. 2005, ISSN: 0957-4158. DOI: `10.1016/j.mechatronics.2005.06.006`. [Online]. Available: `https://www.sciencedirect.com/science/article/pii/S0957415805000760` (visited on 04/09/2021).

[41]   D. Hong, I. Hwang, P. Yoon, and K. Huh, "Development of a Vehicle Stability Control System Using Brake-by-Wire Actuators," en, *Journal of Dynamic Systems, Measurement, and Control*, vol. 130, no. 1, p. 011 008, Jan. 2008, ISSN: 0022-0434, 1528-9028. DOI: `10.1115/1.2807190`. [Online]. Available: `https://asmedigitalcollection.asme.org/dynamicsystems/article/doi/10.1115/1.2807190/417354/Development-of-a-Vehicle-Stability-Control-System` (visited on 04/01/2021).

[42]   D.-H. Kim, J.-M. Kim, S.-H. Hwang, and H.-S. Kim, "Optimal brake torque distribution for a four-wheeldrive hybrid electric vehicle stability enhancement," en, *Proceedings of the Institution of Mechanical Engineers, Part D: Journal of Automobile Engineering*, vol. 221, no. 11, pp. 1357–1366, Nov. 2007, ISSN: 0954-4070, 2041-2991. DOI: `10.1243/09544070JAUTO352`. [Online]. Available: `http://journals.sagepub.com/doi/10.1243/09544070JAUTO352` (visited on 03/31/2021).

[43]   S. Thrun, M. Montemerlo, H. Dahlkamp, *et al.*, "Stanley: The robot that won the darpa grand challenge," *Journal of field Robotics*, vol. 23, no. 9, pp. 661–692, 2006.

[44]   P. Falcone, H. E. Tseng, J. Asgari, F. Borrelli, and D. Hrovat, "Integrated braking and steering model predictive control approach in autonomous vehicles," *IFAC Proceedings Volumes*, vol. 40, no. 10, pp. 273–278, 2007.

[45]   I. Mahtout, F. Navas, D. Gonzalez, V. Milanés, and F. Nashashibi, "Youla-kucera based lateral controller for autonomous vehicle," in *2018 21st international conference on intelligent transportation systems (ITSC)*, IEEE, 2018, pp. 3281–3286.

[46]   H. Atoui, "Switching/interpolating lpv control based on youla-kucera parameterization: Application to autonomous vehicles," Ph.D. dissertation, Université Grenoble Alpes [2020-....], 2022.

[47]   K. Yang, X. Tang, Y. Qin, Y. Huang, H. Wang, and H. Pu, "Comparative study of trajectory tracking control for automated vehicles via model predictive control and robust h-infinity state feedback control," *Chinese Journal of Mechanical Engineering*, vol. 34, no. 1, pp. 1–14, 2021.

[48]   L. Filipozzi, "Next Generation Integrated Vehicle Dynamics and Controls," en, Ph.D. dissertation, University of California, Davis, Davis, CA, USA, 2022.

[49]   J. Wang and S. Shen, "Integrated vehicle ride and roll control via active suspensions," *Vehicle System Dynamics*, vol. 46, no. S1, pp. 495–508, 2008.

[50] A. Soltani, "Low Cost Integration of Electric Power-Assisted Steering (EPAS) with Enhanced Stability Program (ESP)," en, Ph.D. dissertation, Cranfield University, UK, 2014.

[51] S. Karaman and E. Frazzoli, "Incremental sampling-based algorithms for optimal motion planning," *Robotics: Science and Systems VI*, 2010. DOI: `10.15607/rss.2010.vi.034`.

[52] S. M. LaValle, *Planning algorithms*. Cambridge university press, 2006, ch. 5.

[53] M. McNaughton, C. Urmson, J. M. Dolan, and J.-W. Lee, "Motion planning for autonomous driving with a conformal spatiotemporal lattice," *2011 IEEE International Conference on Robotics and Automation*, 2011. DOI: `10.1109/icra.2011.5980223`.

[54] B. Paden, M. Cap, S. Z. Yong, D. Yershov, and E. Frazzoli, "A survey of motion planning and control techniques for self-driving urban vehicles," *IEEE Transactions on Intelligent Vehicles*, vol. 1, no. 1, pp. 33–55, 2016. DOI: `10.1109/tiv.2016.2578706`.

[55] M. Kissai, B. Monsuez, and A. Tapus, "Review of integrated vehicle dynamics control architectures," in *2017 European Conference on Mobile Robots (ECMR)*, 2017, pp. 1–8. DOI: `10.1109/ECMR.2017.8098687`.

[56] H. B. Pacejka, *Tyre and Vehicle Dynamics*. Butterworth-Heinemann, 2012, ISBN: 9780080970165.

[57] H. Dugoff, P. S. Fancher, and L. Segel, "An analysis of tire traction properties and their influence on vehicle dynamic performance," in *International Automobile Safety Conference*, SAE International, Feb. 1970. DOI: `https://doi.org/10.4271/700377`. [Online]. Available: `https://doi.org/10.4271/700377`.

[58] C. C. De Wit, H. Olsson, K. J. Astrom, and P. Lischinsky, "A new model for control of systems with friction," *IEEE Transactions on automatic control*, vol. 40, no. 3, pp. 419–425, 1995.

[59] M. Burckhardt, *Fahrwerktechnik: Radschlupf-Regelsysteme: Reifenverhalten, Zeitablaeufe, Messung des Drehzustands der Raeder, Anti-Blockier-System (ABS), Theorie Hydraulikkreislaeufe, Antriebs-Schlupf-Regelung (ASR), Theorie Hydraulikkreislaeufe, elektronische Regeleinheiten, Leistungsgrenzen, ausgefuehrte Anti-Blockier-Systeme und Antriebs-Schlupf-Regelungen*. Vogel, 1993.

[60] A. Schmeitz, I. Besselink, and S. Jansen, "Tno mf-swift," *Vehicle System Dynamics*, vol. 45, no. S1, pp. 121–137, 2007.

[61] I. Besselink, A. Schmeitz, and H. Pacejka, "An improved magic formula/swift tyre model that can handle inflation pressure changes," *Vehicle System Dynamics*, vol. 48, no. S1, pp. 337–352, 2010.

[62] E. Arasteh, F. Assadian, and L. Filipozzi, "Algorithm to generate target for anti-lock braking system using wheel power," en, *Jr. Mechanical and Aerospace Engineering*, vol. 2, 1 2021. [Online]. Available: `https://auctoresonline.org/article/` `algorithm-to-generate-target-for-anti-lock-braking-system-using-wheel-` `power` (visited on 04/23/2021).

[63] D. Karnopp, D. L. Margolis, and R. C. Rosenberg, *System dynamics: modeling and simulation of mechatronic systems*, 5th ed. Hoboken, NJ: Wiley, 2012, ISBN: 978-0-470-88908-4.

[64] J. Zhao, D. Song, B. Zhu, Z. Chen, and Y. Sun, "Nonlinear Backstepping Control of Electro-Hydraulic Brake System Based on Bond Graph Model," *IEEE Access*, vol. 8, pp. 19 100–19 112, 2020, Conference Name: IEEE Access, ISSN: 2169-3536. DOI: `10.1109/ACCESS.2020.2968513`.

[65] E. Arasteh and F. Assadian, "Bond graph modeling of brake-by-wire actuators on a one-wheel vehicle model," *Society for Modeling and Simulation International*, vol. 53, no. 3, pp. 169–178, 2021.

[66] X. Wang, S. Lin, and S. Wang, "Dynamic Friction Parameter Identification Method with LuGre Model for Direct-Drive Rotary Torque Motor," en, *Mathematical Problems in Engineering*, vol. 2016, pp. 1–8, 2016, ISSN: 1024-123X, 1563-5147. DOI: `10.1155/` `2016/6929457`. [Online]. Available: `http://www.hindawi.com/journals/mpe/2016/` `6929457/` (visited on 04/23/2021).

[67] F. Assadian and K. R. Mallon, *ROBUST CONTROL: Youla parameterization approach.* English. JOHN WILEY, 2021, OCLC: 1031449602, ISBN: 978-1-119-50036-0.

[68] J. Doyle, "Robust and optimal control," in *Proceedings of 35th IEEE Conference on Decision and Control*, vol. 2, 1996, 1595–1598 vol.2. DOI: `10.1109/CDC.1996.572756`.

[69] D. Youla, J. Bongiorno, and H. Jabr, "Modern wiener–hopf design of optimal controllers part i: The single-input-output case," *IEEE Transactions on Automatic Control*, vol. 21, no. 1, pp. 3–13, 1976. DOI: `10.1109/TAC.1976.1101139`.

[70] V. Kučera, "Stability of discrete linear feedback systems," *IFAC Proceedings Volumes*, vol. 8, no. 1, Part 1, pp. 573–578, 1975, 6th IFAC World Congress (IFAC 1975) - Part 1: Theory, Boston/Cambridge, MA, USA, August 24-30, 1975, ISSN: 1474-6670. DOI: `https://doi.org/10.1016/S1474-6670(17)67787-5`. [Online]. Available: `https://www.sciencedirect.com/science/article/pii/S1474667017677875`.

[71] B. D. ANDERSON, "From youla–kucera to identification, adaptive and nonlinear control," *Automatica*, vol. 34, no. 12, pp. 1485–1506, 1998, ISSN: 0005-1098. DOI: `https://doi.org/10.1016/S0005-1098(98)80002-2`. [Online]. Available: `https:` `//www.sciencedirect.com/science/article/pii/S0005109898800022`.

[72] M. Doumiati, O. Sename, L. Dugard, J.-J. Martinez-Molina, P. Gaspar, and Z. Szabo, "Integrated vehicle dynamics control via coordination of active front steering and rear braking," *European Journal of Control*, vol. 19, no. 2, pp. 121–143, 2013.

[73] H. E. Tseng, B. Ashrafi, D. Madau, T. A. Brown, and D. Recker, "The development of vehicle stability control at ford," *IEEE/ASME transactions on mechatronics*, vol. 4, no. 3, pp. 223–234, 1999.

[74] C. Maffezzoni, N. Schiavoni, and G. Ferretti, "Robust design of cascade control," *IEEE Control Systems Magazine*, vol. 10, no. 1, pp. 21–25, 1990. DOI: `10.1109/37.50665`.

[75] "Anti-windup strategies," in *Practical PID Control*. London: Springer London, 2006, pp. 35–60, ISBN: 978-1-84628-586-8. DOI: `10.1007/1-84628-586-0_3`. [Online]. Available: `https://doi.org/10.1007/1-84628-586-0_3`.

[76] M. V. Kothare, P. J. Campo, M. Morari, and C. N. Nett, "A unified framework for the study of anti-windup designs," *Automatica*, vol. 30, no. 12, pp. 1869–1883, 1994, ISSN: 0005-1098. DOI: `https://doi.org/10.1016/0005-1098(94)90048-5`. [Online]. Available: `https://www.sciencedirect.com/science/article/pii/0005109894900485`.

[77] L. Zaccarian and A. R. Teel, "A common framework for anti-windup, bumpless transfer and reliable designs," en, *Automatica*, vol. 38, no. 10, pp. 1735–1744, Oct. 2002, ISSN: 00051098. DOI: `10.1016/S0005-1098(02)00072-9`. [Online]. Available: `https://linkinghub.elsevier.com/retrieve/pii/S0005109802000729` (visited on 10/25/2021).

[78] F. Todeschini, S. Formentin, G. Panzani, M. Corno, S. M. Savaresi, and L. Zaccarian, "Nonlinear Pressure Control for BBW Systems via Dead-Zone and Antiwindup Compensation," en, *IEEE Transactions on Control Systems Technology*, vol. 24, no. 4, pp. 1419–1431, Jul. 2016, ISSN: 1063-6536, 1558-0865. DOI: `10.1109/TCST.2015.2483562`. [Online]. Available: `http://ieeexplore.ieee.org/document/7300395/` (visited on 03/29/2021).

[79] E. Arasteh and F. Assadian, *New Robust Control Design of Brake-by-Wire Actuators*, en. IntechOpen, Nov. 2020, Publication Title: Advanced Applications of Hydrogen and Engineering Systems in the Automotive Industry, ISBN: 978-1-83968-298-8. DOI: `10.5772/intechopen.94581`. [Online]. Available: `https://www.intechopen.com/online-first/new-robust-control-design-of-brake-by-wire-actuators` (visited on 04/21/2021).

[80] E. Arasteh and F. Assadian, "A comparative analysis of brake-by-wire smart actuators using optimization strategies," *Energies*, vol. 15, no. 2, p. 634, 2022.